



**HAL**  
open science

## Multi-band OFDM transmission at 100 Gbps with sub-band optical switching

Erwan Pincemin, Mengdi Song, Julie Karaki, Omid Zia-Chahabi, Thierry Guillosoou, Didier Grot, Gilles Thouenon, Christophe Betoule, Rémi Clavier, A. Poudoulec, et al.

► **To cite this version:**

Erwan Pincemin, Mengdi Song, Julie Karaki, Omid Zia-Chahabi, Thierry Guillosoou, et al.. Multi-band OFDM transmission at 100 Gbps with sub-band optical switching. *Journal of Lightwave Technology*, 2014, 32 (12), pp.2202-2219. 10.1109/JLT.2014.2322517 . hal-01190705

**HAL Id: hal-01190705**

**<https://hal.science/hal-01190705>**

Submitted on 29 Apr 2022

**HAL** is a multi-disciplinary open access archive for the deposit and dissemination of scientific research documents, whether they are published or not. The documents may come from teaching and research institutions in France or abroad, or from public or private research centers.

L'archive ouverte pluridisciplinaire **HAL**, est destinée au dépôt et à la diffusion de documents scientifiques de niveau recherche, publiés ou non, émanant des établissements d'enseignement et de recherche français ou étrangers, des laboratoires publics ou privés.



Distributed under a Creative Commons Attribution - NonCommercial 4.0 International License

# Multi-Band OFDM Transmission at 100 Gbps With Sub-Band Optical Switching

Erwan Pincemin, M. Song, J. Karaki, O. Zia-Chahabi, T. Guillossou, D. Grot, G. Thouenon, C. Betoule, R. Clavier, A. Poudoulec, M. Van der Keur, Y. Jaouën, R. Le Bidan, T. Le Gall, P. Gravey, M. Morvan, B. Dumas-Feris, M. L. Moulinard, and G. Froc

**Abstract**—In this paper, we present an original work on sub-wavelength optical switching performed over a coherent multi-band orthogonal frequency-division multiplexing (MB-OFDM) super-channel operating at 100 Gbps. After having demonstrated that dual-polarization MB-OFDM (DP-MB-OFDM) is as efficient as single-carrier dual-polarization quaternary phase shift keying (DP-QPSK) technology to transport 100 Gbps data-rate over a  $10 \times 100$ -km G.652 fiber-based transmission line, we show that optical add-drop of OFDM sub-bands as narrow as 8 GHz inside a 100 Gbps DP-MB-OFDM signal constituted of four sub-bands is feasible in the middle of this 1000-km transmission line. The flexible optical add-drop multiplexer (FOADM) implemented here is constituted by the association of an ultra-narrow pass-band and stop-band optical filter. The design and realization of such ultra-selective optical filters is presented, while the impact of their physical features over the quality of transmission is discussed. To prove that several add-drop multiplexers can be cascaded, our FOADM is introduced into a G.652 fiber-based recirculating loop and the impact of the cumulated filtering transfer function as well as the crosstalk inside the OADM are investigated. A typical use case for the introduction of such FOADM into long-haul transport networks is given, and the capital expenditure (CAPEX) cost advantage for the multi-layer transport networks is highlighted. By the proof of concept delivered here, combination of super-channel and sub-wavelength optical switching pushes network flexibility far away of what is today proposed by system vendors, opening new horizons for an optimized use of multi-layer transport networks.

**Index Terms**—CAPEX cost, DP-QPSK, MB-OFDM, sub-wavelength optical switching, 100 Gbps WDM transmission.

E. Pincemin, M. Song, O. Zia-Chahabi, T. Guillossou, D. Grot, G. Thouenon, C. Betoule, and R. Clavier are with the Orange Labs Networks, 22307 Lannion, France (e-mail: erwan.pincemin@orange.com; mengdi.song@orange.com;omid.ziachahabi@orange.com; thierry.guillossou@orange.com; didier.grot@orange.com; gilles.thouenon@orange.com; christophe.betoule@orange.com; remi.clavier@orange.com).

A. Poudoulec and M. Van der Keur are with the Yenista Optics, 22300 Lannion, France (e-mail: alain.poudoulec@yenista.com; michiel.vanderkeur@yenista.com).

Y. Jaouën is with the Institut Mines Telecom, Telecom ParisTech, 75634 Paris, France (e-mail: yves.jaouen@telecom-paristech.fr).

R. Le Bidan, J. Karaki, T. Le Gall, P. Gravey, M. Morvan, B. Dumas-Feris, and M. L. Moulinard are with the Institut Mines Telecom, Telecom Bretagne, Technopôle Brest-Iroise, 29238 Brest Cedex 3, France (e-mail: raphael.lebidan@telecom-bretagne.eu; julie.karaki@telecom-bretagne.eu; thierry.legall@telecom-bretagne.eu; philippe.gravey@telecom-bretagne.eu; michel.morvan@telecom-bretagne.eu; barbara.dumasferis@telecom-bretagne.eu; marielaure.moulinard@telecom-bretagne.eu).

G. Froc is with the Mitsubishi Electric Research Center Europe, 35000 Rennes, France (e-mail: gfroc@merce.fr).

## I. INTRODUCTION

IN the next generations of optical transport networks, flexibility will be carried out to a high degree of efficiency, in order to increase significantly the capacity transported by the fiber bandwidth but also to optimize as much as possible the aggregation process through the various network layers (from optical to IP layer). Indeed, the filling of the communication connections into a network is dimensioned for the peak of traffic and not for the average data-rate, involving a traffic over-provisioning of  $\sim 45\%$  [1]. The idea is thus to perform an optimization of the multi-layer transport network architecture in order to deploy only the equipments that are necessary. That starts by introducing flexibility into the optical layer of the network [2], and in particular by performing sub-wavelength optical switching over the up-coming super-channels. The proposed scheme consists in operating an optical separation-aggregation of the independent sub-bands which constitute the super-channels thanks to the use of ultra-selective optical pass-band and stop-band filters [3], [4]. To push farther the flexibility, the idea would be also to adapt the capacity carried by the sub-bands to the services that are transported. For instance and as illustrated in the lower part of the Fig. 1 below, the data-rates carried by each sub-wavelength could take the following values: 12.5, 25, 33.3, 50, 66.6 and 100 Gbps. By using the MB-OFDM technique, this bit-rate elasticity would be obtained by playing both over the modulation format transported by the sub-carriers constituting the OFDM sub-bands (i.e., BPSK, QPSK, 8-QAM, 16-QAM), and over the number of sub-carriers constituting each OFDM sub-band (or equivalently over their bandwidth).

According to us and as demonstrated in this manuscript, MB-OFDM is the preferred candidate to achieve such a high degree of flexibility. Indeed, thanks to its rectangular spectrum and the possibility to easily pre-distort electronically its profile (to take into account for instance the distortion induced by the OADM cascade), OFDM is naturally robust to ultra-narrow optical filtering. From its side, Nyquist-WDM super-channel at 32 Gbauds seems particularly sensitive to 37.5-GHz optical filtering [5], [6]. Furthermore, the opportunity to play both on the modulation format and bandwidth (or equivalently on the number of sub-carriers) of each OFDM sub-band gives the

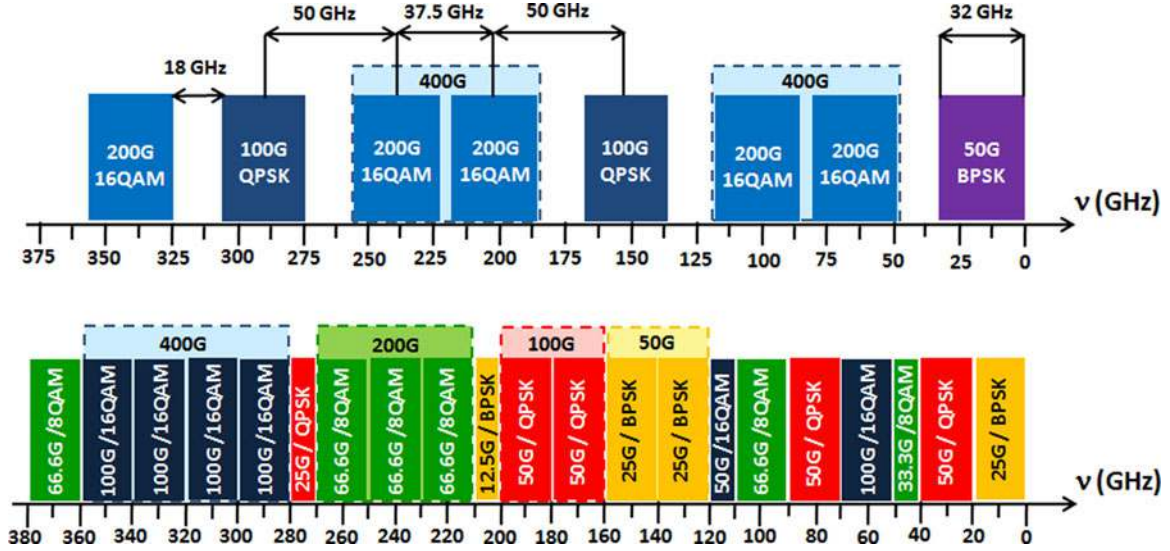


Fig. 1 Bandwidth management proposed today by the Nyquist-WDM super-channel working at 32 Gbaud and the mixed 37.5/50 GHz spectral grid approach (upper figure part), and by the MB-OFDM technology and the grid-less management of the fiber bandwidth approach (lower figure part).

means to better manage the fiber bandwidth and to limit as much as possible the gaps which are created inside the spectrum. Note that this fiber bandwidth management is less easy to achieve with the Nyquist-WDM technology operating at a constant baud-rate, as proposed today by the equipment suppliers [7]–[9]. Fig. 1 below compares the short-term approach of flexibility proposed today by the system vendors, based on the combination of Nyquist-WDM super-channel at 32 Gbauds and mixed 37.5/50-GHz spectral grid [5]–[10], and our MB-OFDM approach, based on the implementation of MB-OFDM technique and gridless management of the fiber bandwidth. In the short-term approach, the sub-bands inside the Nyquist-WDM super-channel are spaced by 37.5 GHz, the guard-band between the WDM channels is typically of  $\sim 18$  GHz, and the capability to optically switch the sub-bands inside the super-channel is not authorized. The data-rate carried by the WDM channels are either 50 Gbps (with BPSK), 100 Gbps (with QPSK), 200 Gbps (with 16-QAM), or 400 Gbps for the super-channel grouping two 200 Gbps 16-QAM sub-bands [7]–[9]. In our MB-OFDM approach, the spectral granularity for the OFDM sub-bands is 10 GHz, the OFDM sub-bands occupy a spectral slot of 10 or 20 GHz and can be grouped together to constitute a super-channel transporting 50, 100, 200, or 400 Gbps (as shown in Fig. 1 below). Note that we have deliberately chosen a spectral granularity (10 GHz) which is different from the one defined in the standards (12.5 GHz), in order to illustrate more concretely what is the gridless approach. Thanks to the use of ultra-narrow optical pass-band and stop-band filters, the optical add-drop of OFDM sub-bands is allowed. The guard-band between the OFDM sub-bands is typically of  $\sim 2$ – $4$  GHz (as shown later in this paper). With this scheme, the adaptability of the optical layer to the services transported is very high and the management of spectral gaps in the fiber bandwidth is greatly eased by the flexibility provided by the OFDM format. Note however that a certain complexity is associated with this proposed

flexibility scheme, as the performance of Nyquist-WDM or MB-OFDM sub-bands in terms of maximum transmission distance depends on the modulation format implemented within each sub-band.

In this paper, we present an original work on sub-band optical switching performed over a coherent MB-OFDM super-channel operating at 100 Gbps. In Section I, we detail how the coherent MB-OFDM signal is generated and detected. In particular, we describe the main steps of the digital signal processing (DSP) operated at the transmitter and receiver side. In Section II, we compare the transmission performance of our 100 Gbps MB-OFDM super-channel constituted of four polarization-multiplexed sub-bands with that of single-carrier 100 Gbps DP-QPSK over an uncompensated  $10 \times 100$ -km G.652 fiber-based transmission line. In Section III, the design and realization of the ultra-narrow optical filters required for the “add-drop” process is discussed, and the obtained profiles for both the pass-band and stop-band filters are presented. In Section IV, the assessment of the efficiency of our FOADM to add-drop OFDM sub-bands as narrow as 8 GHz inside the 100 Gbps MB-OFDM super-channel is carried out both in back-to-back and in the previously introduced 1000-km transmission line [4]. In particular, the bandwidths of the “drop” and “notch” filters used into the FOADM are optimized as a function of the guard-band separating two consecutive sub-channels. In Section V, the question of the cascability of the FOADM is studied thanks to the insertion of the add-drop multiplexer into a  $2 \times 100$ -km G.652 fiber-based recirculating loop. The impact of the cumulated filtering transfer function, as well as the crosstalk inside the FOADM, is investigated. Finally, in the last part of the paper, a typical use case for the FOADM introduction into a long-haul transport network is discussed, and the capital expenditure (CAPEX) cost advantage of MB-OFDM and sub-band optical switching techniques for multi-layer transport networks is highlighted.

## II. COHERENT OFDM: GENERATION AND DETECTION

In this section, we first describe the transmitter and receiver architecture for the generation and detection of a single-band coherent optical OFDM signal. We then introduce the experimental setup used to build a 100 Gbps MB-OFDM signal from four independent 25 Gbps OFDM sub-bands.

### A. Single-Band Coherent OFDM Transmitter Architecture

The basic idea behind OFDM is the sharing of a high bit-rate data stream between a high number (in general, several hundreds) of low bit-rate tributaries transported each by one sub-carrier [11]–[15]. The essential operation of OFDM is the inverse fast Fourier transform (IFFT) which permits to superimpose temporally into one OFDM symbol the symbols transported by the previously introduced sub-carriers, at the transmitter side. The number of time-domain samples into the created OFDM symbol is then equal to the number of sub-carriers that feed the IFFT. Fig. 2 presents the block diagram of a typical OFDM transmitter and receiver. A high bit-rate binary data stream is first split into a high number of low bit-rate binary data tributaries by a serial-to-parallel conversion. After conversion of these binary data streams into quadrature amplitude modulation (QAM) symbols, some training symbols and sub-carriers (named pilot tones) are introduced for channel and phase noise estimation/correction (performed at the receiver side). As already explained, the IFFT permits to superimpose temporally into one OFDM symbol the QAM symbols carried by the low symbol-rate tributaries, while their orthogonality is ensured by spacing the sub-carriers of a value inversely proportional to the symbol duration. Orthogonality can be declined into the spectral or temporal domain. In the spectral domain, orthogonality is guaranteed by the sub-carrier spacing equal to a multiple of the inverse of the symbol duration, as well as by the sinc spectrum of the OFDM sub-carriers. This sinc profile ensures that sub-carriers will not interfere after demodulation and will not be affected by inter-carrier interference (ICI). Orthogonality in the time domain is guaranteed by the presence of an integer number of cycles into the OFDM symbol for each of the considered OFDM sub-carriers. A cyclic prefix (or guard interval) is then added to the beginning of each OFDM symbol in order to prevent inter-symbol interference (ISI) over time-dispersive channels. The cyclic prefix is formed by the copy of the last samples of the OFDM symbol, the number of samples being determined by the maximum channel delay spread. Clipping is then performed in order to suppress the peaks of amplitude, which affect the OFDM signal and could result into an inefficient use of the dynamic range of the digital-to-analogue converters (DAC). Spectral pre-emphasis is also carried out to compensate for the non-flat frequency response of DAC, low-pass frequency filter (LPF) and RF driver. A parallel-to-serial conversion is then applied to obtain the in-phase (I) and quadrature (Q) components of the OFDM signal. The I/Q tributaries feed a pair of DAC embedded into an arbitrary waveform generator (AWG), whose 3-dB bandwidth and sampling speed are equal to  $\sim 10$  GHz and 12 GSamples/s, respectively. LPF are applied at the DAC outputs to remove the aliasing products produced by the sampling

process. RF drivers operating in their linear regime feed a complex Mach-Zehnder modulator (MZM), which optically mixes together the I and Q data streams. An external cavity laser (ECL) with 100-kHz linewidth feeds the complex MZM, which is itself connected to a polarization-division-multiplexing (PDM) unit. The role of this PDM unit is to generate the dual-polarization OFDM signal at a reasonable cost. It consists in replicating the OFDM signal and in delaying the two copies by one symbol delay. A variable optical attenuator (VOA) inserted into the lower arm of the PDM unit equilibrates the power of each of the two OFDM replicas, which are coupled by the means of a polarization beam combiner (PBC). The polarization extinction ratio of each OFDM replica is increased by polarizers embedded into the lower and upper arms of the PDM unit.

### B. Single-Band Coherent Optical OFDM Receiver Architecture

At the receiver side, as shown in the lower part of Fig. 2, a polarization beam splitter (PBS) separates the polarization-multiplexed OFDM signal in its two components, carried respectively by the X and Y polarizations. For each of these two polarization components, a  $90^\circ$  hybrid firstly mixes together the local oscillator (LO) and the OFDM signal, and secondly separates the I and Q tributaries. Four balanced photodiodes detect the  $I_X$ ,  $Q_X$ ,  $I_Y$  and  $Q_Y$  data streams, which are sent over four analog-to-digital converters (ADC) embedded into a real-time storage oscilloscope working at 50 GSamples/s.

The DSP at the receiver side is then performed in order to compensate for system as well as propagation impairments and recover the binary data sent over the X and Y polarizations. The expression of the two time-domain samples  $\underline{x}_{nj}$  received over the X and Y polarizations at relative time index  $n$  within OFDM symbol  $j$  can be written in vector form as:

$$\underline{x}_{nj} = e^{i \left( 2\pi \Delta_{\text{CFO}} \cdot (j(N_{\text{SC}} + N_g) + n) \frac{1}{f_s} + \varphi_{nj} \right)} \times \sum_{l=0}^{L_m-1} \underline{h}(l) * \underline{x}_{(n-l-p)j} + \underline{n}_{nj}$$

$\Delta_{\text{CFO}}$  is the carrier frequency offset (CFO) between the LO and the laser used into the transmitter,  $N_{\text{sc}}$  is the number of OFDM sub-carriers,  $N_g$  is the cyclic prefix length,  $f_s$  is the DAC/ADC sampling frequency,  $\varphi_{nj}$  is the laser phase noise,  $\underline{h}$  is the channel impulse response having at most  $L_m$  discrete paths,  $\underline{x}_{nj}$  are the transmitted time-domain samples at time index  $n$  within OFDM symbol  $j$ ,  $p$  is an integer timing offset, and  $\underline{n}_{nj}$  is the amplified spontaneous emission noise.

Timing synchronization is first implemented in order to determine the start of the OFDM symbol. Timing errors will cause the FFT window to be applied at an incorrect location in the received signal, resulting in both ISI and ICI, and leading to a severe degradation of the system performance. Hereafter, we use synchronization algorithms based on the insertion of a training symbol constituted by the L-fold repetition of a pre-determined basic pattern B, possibly with alternation of signs. Schmidl and Cox [16], Minn and Barghava [17] and Shi and Serpedin [18]

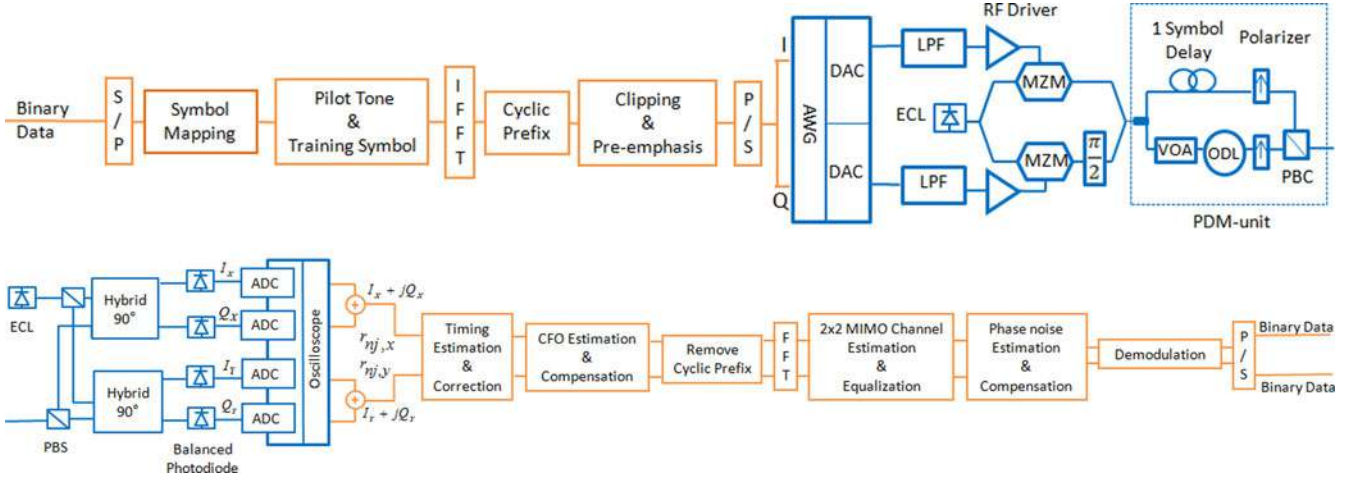


Fig. 2 Block diagram of a typical OFDM transmitter (upper figure part) and receiver (lower figure part), with S/P = Serial-to-Parallel Conversion, IFFT = Inverse Fast Fourier Transform, P/S = Parallel-to-Serial Conversion, AWG = Arbitrary Waveform Generator, DAC = Digital-to-Analogue Converter, LPF = Low-Pass Filter, ECL = External Cavity Laser, MZM = Mach-Zehnder modulator, VOA = Variable Optical Attenuator, OD = Optical Delay Line, PBC = Polarization Beam Combiner, PBS = Polarization Beam Splitter, ADC = Analog-to-Digital Converter, CFO = Carrier Frequency Offset, FFT = Fast Fourier Transform, MIMO = Multiple-Input-Multiple-Output.

algorithms use training symbols of the form:  $[+B, +B]$ ,  $[+B +B +B -B]$ , and  $[+B +B -B +B]$ , respectively. Accordingly, the received signal is correlated with itself over a sliding window of appropriate length in order to find the repeated patterns and to locate the start of the training symbol. This is done by maximizing a metric of the form

$$M(p) = \max_p \left\{ \frac{|K(p)|}{E(p)} \right\}$$

where  $K$  is an appropriate auto-correlation metric,  $E$  is an energy normalization metric, and  $p$  ranges over the admissible time index. In the following, the Minn and Barghava algorithm has been chosen for its accuracy.

Compensation of CFO between the LO and the laser used into the transmitter is the second DSP step. Generally, CFO results in a phase offset common to all the sub-carriers of a given symbol, in a complex attenuation common to all the sub-carriers and symbols, and in ICI. While the two first effects can be corrected, ICI is very detrimental and cannot be compensated. In order to constrain CFO to a relatively low value and avoid too much ICI, the wavelength of the LO has to be tuned to match (at least approximately) the wavelength of the ECL used at the transmitter side. The technique used to coarsely tune the LO can be decomposed in two steps: firstly, the spectrum of the data sampled by the ADC is generated by Fourier transform; secondly, the base-band spectrum of the OFDM signal originally emitted is recovered by shifting the wavelength of the LO accordingly. The usual approach for CFO compensation is then to decompose CFO into its fractional and integer part. The determination of the fractional part reuses the training symbol previously defined for synchronization. If  $L$  denotes the number of repetitions of the basic pattern  $B$  into the training symbol, an accurate CFO estimate  $\Delta_{\text{CFO}}$  can be obtained by averaging  $\Delta_{\text{CFO}}$  over the  $N_{\text{sc}}/L$  samples of the basic pattern  $B$ . The following expression

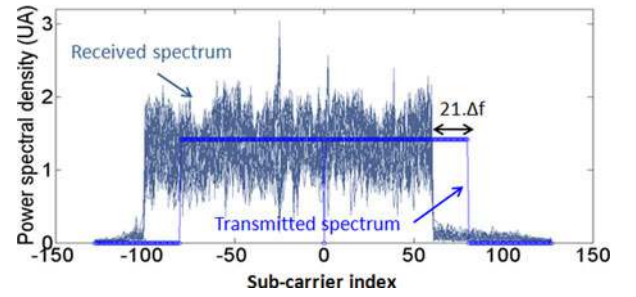


Fig. 3 Power spectral density versus sub-carrier index for the transmitted and received OFDM signal, with an integer CFO measured at  $-21\Delta f$ .

is then obtained for the fractional CFO part:

$$\Delta_{\text{CFO}} = \frac{L}{2} \cdot \frac{f_s}{N_{\text{sc}}} \cdot \arg \left( \frac{L}{N_{\text{sc}}} \sum_{n=0}^{N_{\text{sc}}/L - 1} r_{nj}^* r_{(n+1) \cdot \frac{N_{\text{sc}}}{L} j} \right).$$

The estimation of the integer CFO part is carried out by recovering the spectrum of the data over the X and Y polarizations through a discrete Fourier transform (DFT). By comparing the recovered spectrum at the receiver side with the original spectrum generated at the transmitter side, it is straightforward to determine the integer CFO [19]. Fig. 3 below illustrates this method. In this example, the integer CFO estimated by comparing the spectrum obtained after DFT at the transmitter and receiver side is equal to  $-21\Delta f$  ( $\Delta f$  denoting the sub-carrier spacing).

After removal of the cyclic prefix, the OFDM signal is converted back to the frequency domain by fast Fourier transform (FFT). Channel estimation and equalization is then performed. Its role is to compensate for the gain/phase distortion experienced by the sub-carriers, as well as to carry out polarization separation.

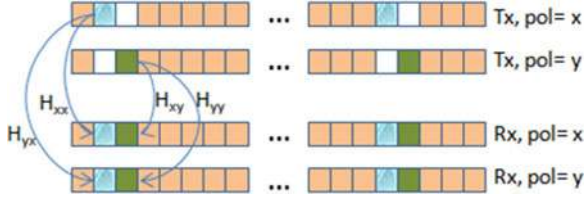


Fig. 4 Particular structure of the training symbols used for channel estimation and equalization, in the case of a dual-polarization OFDM system.

The channel estimate is computed by using the training symbols and by supposing that the data symbols are disturbed by the same impairments than the training symbols.  $2 \times 2$  multiple-input-multiple-output (MIMO) least square channel estimation is implemented. We reuse here a special structure for the training symbols, which has been proposed in [15], [20] and is depicted in Fig. 4 above. It consists in transmitting two training symbols on each polarization, for instance twice in the duration of the OFDM frame (as illustrated in Fig. 4). One arbitrary OFDM symbol (in blue over Fig. 4) followed by an empty symbol is sent over the X polarization, while an empty symbol followed by another arbitrary OFDM symbol (in green over Fig. 4) is launched over the Y polarization. In a dual-polarization OFDM system, the signal received on each polarization is a linear combination of the two polarization-multiplexed transmitted signals. Specifically, for a given sub-carrier  $k$ ,  $H_{xx}(k)$  and  $H_{yx}(k)$  represent the energy transferred from the transmitted polarization X towards the received polarizations X and Y, respectively. Similarly,  $H_{xy}(k)$  and  $H_{yy}(k)$  represent the energy transferred from the transmitted polarization Y towards the received polarizations X and Y, respectively. For our two previously defined training symbols  $[c_{kj} \ 0]$  over the X polarization and  $[0, c_{k(j+1)}]$  over the Y polarization, the received symbols  $[R_{kj} \ R_{k(j+1)}]$  in the frequency domain on each sub-carrier  $k$  are given by

$$\begin{bmatrix} R_{kj,x} & R_{k(j+1),x} \\ R_{kj,y} & R_{k(j+1),y} \end{bmatrix} = \begin{bmatrix} H_{xx}(k) & H_{xy}(k) \\ H_{yx}(k) & H_{yy}(k) \end{bmatrix} \cdot \begin{bmatrix} c_{kj,x} & 0 \\ 0 & c_{k(j+1),y} \end{bmatrix}.$$

The four elements of the  $\underline{H}$  matrix are then easily obtained by

$$\begin{aligned} H_{xx}(k) &= \frac{R_{kj,x}}{c_{kj,x}} & H_{xy}(k) &= \frac{R_{k(j+1),x}}{c_{k(j+1),y}} \\ H_{yx}(k) &= \frac{R_{kj,y}}{c_{kj,x}} & H_{yy}(k) &= \frac{R_{k(j+1),y}}{c_{k(j+1),y}}. \end{aligned}$$

Zero-forcing (ZF) equalization is used. It has the double advantage of not requiring any other knowledge than the channel frequency response, and more importantly of being optimal for optical channels whose frequency response has unit magnitude ( $|H_k| = 1$ ), thereby avoiding the classical problem of noise enhancement. The  $2 \times 2$  MIMO ZF equalizer output can then be written as

$$\hat{\underline{R}}_{kj} = \underline{H}_k^{-1} \times \underline{R}_{kj}$$

where  $\underline{H}_k^{-1}$  is the inverse of the  $2 \times 2$  channel frequency response (or, in practice, its estimate) for the sub-carrier  $k$ .

The last processing to perform is the compensation of the laser phase noise, which constitutes a major impairment for the performance of OFDM systems. By decomposing the phase noise  $\phi_{n,j}$  into a mean rotation  $\langle \phi_j \rangle$  and a random fluctuation  $\Delta \phi_{n,j}$  around the mean, the received signal  $\underline{R}_{kj}$  in the frequency domain at the DFT output can be written as

$$\begin{aligned} \underline{R}_{kj} &= \underbrace{\left( \sum_{n=0}^{N_{SC}-1} e^{i\langle \phi_j \rangle} \right)}_{\alpha_j e^{i\langle \phi_j \rangle}} \underline{H}_k \underline{c}_{kj} \\ &+ \underbrace{\sum_{n=0}^{N_{SC}-1} e^{i\Delta \phi_{n,j}} \sum_{\substack{l=0 \\ l \neq k}}^{N_{SC}-1} \underline{H}_l \underline{c}_{lj}}_{ICI} e^{-i2\pi \cdot \frac{n(1-k)}{N_{SC}}}. \end{aligned}$$

Laser phase noise has two kind of effect on the OFDM signal. First, it results in an attenuation  $\alpha_j$  and a phase shift  $\langle \phi_j \rangle$ , which impairs all the sub-carriers in the symbol  $j$  and differs from one symbol to the other. Second, it involves ICI. If we assume that the phase noise trajectory slowly evolves around its mean value along the OFDM symbol, and neglect the small fluctuations  $\Delta \phi_{n,j}$ , then  $\alpha_j \sim 1$  and ICI can be neglected. Only the common phase error (CPE) term  $\langle \phi_j \rangle$  has to be considered and corrected [21]. CPE estimation is performed here thanks to the pilot tone method. It allows correcting the phase rotation common to all the sub-carriers in an OFDM symbol. After extraction of the pilot tones for each OFDM symbol  $j$ , the phase difference between the received pilot sub-carriers and the transmitted ones is evaluated. The CPE term  $\langle \phi_j \rangle$  affecting the OFDM symbol  $j$  is estimated by averaging the phase difference over the pilot tones

$$\exp(i\langle \phi_j \rangle) = \frac{1}{N_p} \sum_{k \in I} \frac{\hat{R}_{kj} \times |c_{kj}|}{c_{kj} \times |\hat{R}_{kj}|}$$

where  $I$  is the set of pilot tone indices,  $N_p$  is the number of pilot tones,  $\hat{R}_{kj}$  is the equalizer output for the pilot tone of index  $k$ , and  $c_{kj}$  is the known transmitted symbol on this pilot tone. The CPE is finally corrected by multiplying each OFDM symbol by the conjugate of the previously introduced estimated CPE complex exponential function

$$\hat{c}_{kj} = \hat{R}_{kj} \cdot \exp(-i \cdot \langle \phi_j \rangle).$$

### C. Generation of the 100 Gbps Multi-Band OFDM Signal

We are now describing in detail how the 100 Gbps coherent DP-MB-OFDM signal is generated experimentally. We first explain how one polarization-multiplexed OFDM sub-band carrying 25 Gbps is produced [22]. The two DAC of a Tektronix 7122B arbitrary waveform generator operating at a sampling rate of 12 GSamples/s generate the I and Q tributaries of the OFDM signal, which have both a bandwidth of  $\sim 4$  GHz. 256 sub-carriers constitutes the OFDM signal. Each OFDM sub-carrier is modulated by a QPSK constellation. A first sequence of training symbols  $[0 \ \text{TS1}]$  is inserted at the frame beginning

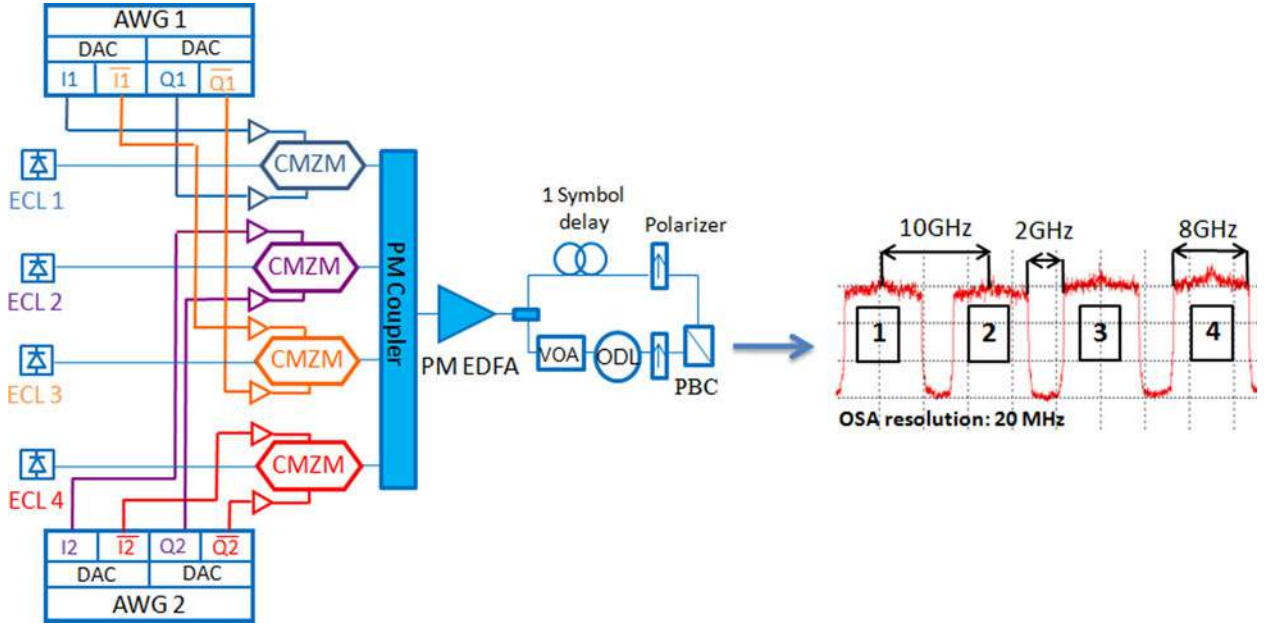


Fig. 5 Set-up of the 100 Gbps DP-MB-OFDM transmitter. In inset is shown the spectrum of the 100 Gbps DP-MB-OFDM signal. OSA = Optical Spectral Analyzer, PM = Polarization-Maintaining, PM-EDFA = Polarization-Maintaining Erbium-doped fiber amplifier.

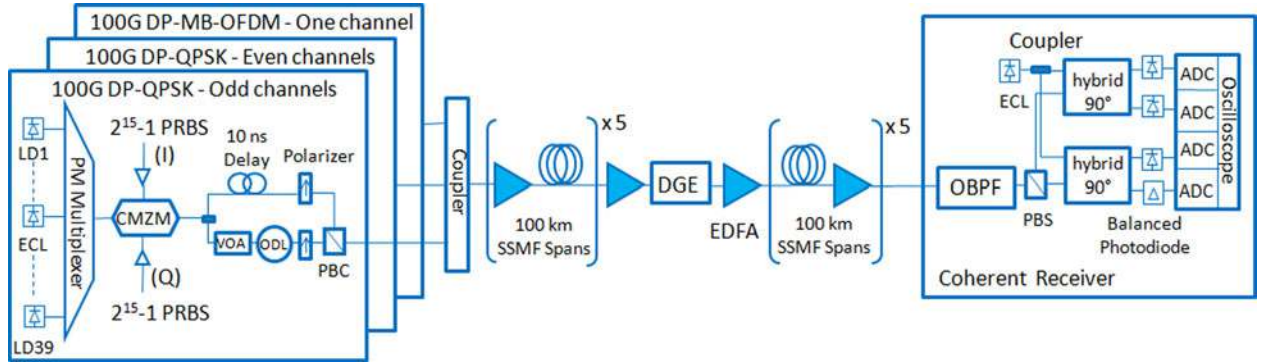


Fig. 6 Set-up of the  $10 \times 100$ -km transmission test-bed, with the 124.4 Gbps DP-MB-OFDM channel, the 79 odd and even 112 Gbps DP-QPSK wavelengths, the  $10 \times 100$ -km uncompensated G.652 SSMF transmission line, and the coherent receiver. LD = Laser Diode, PRBS = Pseudo-Random Bit Sequence, SSMF = Standard Single-Mode Fiber, DGE = Dynamic Gain Equalizer, OBPF = Optical Band-Pass Filter.

for synchronization and CFO estimation. A second sequence of five training symbols with the following structure [0 TS2 0 TS2 0] is inserted in order to carry out channel estimation and equalization (including polarization separation). Six pilot tones are dedicated to phase noise compensation. A cyclic prefix of 18 samples (1.4 ns) is added at the beginning of each OFDM symbol to provide robustness against ISI, and more particularly against chromatic dispersion as high as 17000 ps/nm at 1550 nm. At the DAC outputs, the I and Q signals are filtered by two 4-GHz bandwidth LPF, that suppress the aliasing products generated by the DAC. After amplification by two linear RF drivers, the I and Q tributaries are mixed together by means of a CMZM. The polarization-multiplexed OFDM signal is obtained owing to the previously described PDM unit. The payload data rate is 25 Gbps. The 7% overhead required for forward error correction (FEC), 7% for cyclic prefix, 6% for training symbols,

2.3% for pilot tones lead to a global data rate of 31.1 Gbps for one OFDM sub-band. The bandwidth occupied by the OFDM signal in the optical domain is equal to  $\sim 8$  GHz. The payload data rate of 100 Gbps, increased up to 124.4 Gbps to account for the previous overheads, is obtained through the combination of four dual-polarization OFDM sub-bands. Fig. 5 below shows the transmitter set-up. Our 100 Gbps DP-MB-OFDM signal is generated thanks to four 100-kHz linewidth ECLs spaced by 10 GHz, which feed four CMZM. By means of two AWG, data carried by the neighboring sub-bands are totally de-correlated, provided that the AWG 1 generates the first and third sub-bands while the AWG 2 generates the second and fourth sub-bands. The combination of AWG and CMZM produces the four required OFDM sub-bands of 8-GHz bandwidth each, which are then assembled by a 4:1 polarization-maintaining (PM) coupler, before entering into the PDM unit. A polarization-maintaining

Erbium-doped fibre amplifier (PM-EDFA) balances the transmitter losses. The spectrum of our 100 Gbps DP-MB-OFDM signal measured with a high-resolution (20 MHz) optical spectral analyzer (OSA) is shown in the inset of Fig. 5.

### III. DP-MB-OFDM AND DP-QPSK TRANSMISSION

Before inserting our FOADM into the transmission test-bed, we first evaluate the ability of coherent DP-MB-OFDM technology to transport 100 Gbps over a  $10 \times 100$ -km G.652 fiber-based transmission line. We compare its performance with that of 100 Gbps DP-QPSK. Our previously described 124.4 Gbps DP-MB-OFDM transmitter operating at 1552.93 nm is combined with a multiplex of 79 wavelengths spaced by 50 GHz and modulated at 112 Gbps by DP-QPSK (to take into account the 7% FEC overhead). The 100 Gbps DP-QPSK channel used here as a reference is fed by a 100-kHz linewidth ECL at 1548.11 nm (to limit the impact of laser phase noise), while the 78 other channels ranging from 1529.16 to 1560.61 nm are fed by cheap standard laser diodes (LD). Decorrelated  $2^{15}-1$  pseudo-random bit sequences (PRBS) are used to drive the I and Q ports of the CMZM which generates the QPSK constellation. A 10-ns timing delay is introduced between the two replica of the QPSK signal inside the PDM unit, in order to generate the DP-QPSK signal. The 112 Gbps DP-QPSK odd and even channels are separately multiplexed, independently modulated, and combined with the 124.4 Gbps DP-MB-OFDM signal, before being injected into the optical link. The optical link is constituted of 10 spans of G.652 standard single-mode fiber (SSMF), separated by Erbium-doped fibre amplifiers (EDFA) with 20 dB gain and 5.5 dB noise figure (NF). In the middle of our transmission line, a dynamic gain equalizer (DGE) is inserted in order to flatten the multiplex power after 1000-km. This uncompensated transmission configuration is realistic of the 100 Gbps WDM systems which are today deployed by operators and which presents the best performance, when compared to legacy dispersion-managed systems [7], [8].

At the receiver side, the DP-MB-OFDM and DP-QPSK signals are selected by a square flat-top optical band-pass filter (OBPF) of 0.4 nm bandwidth, and detected by a polarization diversity coherent receiver using a  $\sim 100$ -kHz bandwidth ECL as LO. The signals are converted back to the digital domain thanks to four ADC operating at 50 GSamples/s and embedded into a Tektronix DPO 72004C real-time storage oscilloscope. In the DP-MB-OFDM case, the LO wavelength is tuned to the centre of the OFDM sub-band under measurement, while the DSP is the one described in part II. In the DP-QPSK case, DSP is based on blind equalization, and more particularly on the constant modulus algorithm which carries out polarization separation and residual chromatic dispersion compensation [23]. The fixed part of chromatic dispersion is compensated thanks to two finite-impulse response filters located on the X and Y polarizations [24], respectively. CFO compensation and carrier phase estimation are carried out by the methods described in [25] and [26], respectively. To avoid cycle slips, coherent detection followed by differential decoding is used. Bit-error rates (BER) are evaluated by launching several tens of successive acquisitions

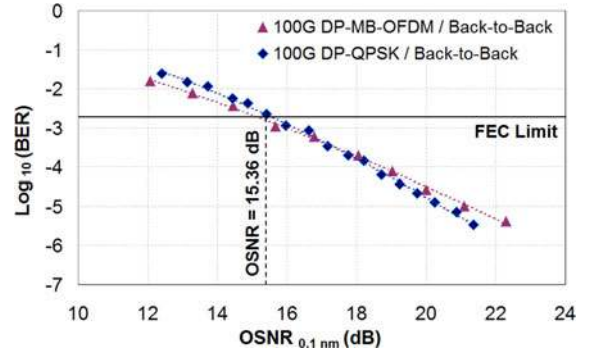


Fig. 7 BER versus OSNR (in 0.1 nm) of the 100 Gbps DP-MB-OFDM and 100 Gbps DP-QPSK modulation formats in the back-to-back configuration. The FEC limit is reached for an OSNR (in 0.1 nm) = 15.36 dB.

and by averaging the corresponding BER. In the OFDM case, 400 acquisitions are carried out and 125 OFDM symbols on each polarization are saved at each acquisition. BER is thus calculated by using 25.6 millions of QPSK symbols (125 OFDM symbols  $\times$  256 sub-carriers  $\times$  2 polarizations  $\times$  400 acquisitions). In the DP-QPSK case, 50 acquisitions are performed and 1.12 millions of QPSK symbols on each polarization are saved at each acquisition. BER is thus calculated by using 112 millions of QPSK symbols (1.12 millions symbols  $\times$  2 polarizations  $\times$  50 acquisitions).

In Fig. 7, the bit-error rate (BER) of DP-MB-OFDM and DP-QPSK is measured as a function of the optical signal-to-noise ratio (OSNR) in 0.1 nm, in the back-to-back configuration. We note that the two curves are nearly superimposed, showing that the quality of our experimental implementation of 100 Gbps DP-MB-OFDM is quite good, and ensuring that the transmission comparison between the two modulation formats will not be impacted by limitations of the DP-MB-OFDM transmitter/receiver. Furthermore, the FEC limit (fixed here at a  $\text{BER} = 2 \times 10^{-3}$ ) is reached for an OSNR in 0.1 nm equal to 15.36 dB for both 100 Gbps DP-MB-OFDM and 100 Gbps DP-QPSK. The  $10 \times 100$ -km uncompensated transmission line is now inserted between the transmitter and the coherent receiver. The transmission performance is measured in different configurations for the two modulation formats under study. In the single-channel (SC) configuration, the channels are not modulated any more, except the DP-MB-OFDM channel at 1552.93 nm and the DP-QPSK channel at 1548.11 nm. The WDM configuration corresponds to the experiment depicted at the beginning of the paragraph III. Fig. 8 shows the BER evolution as a function of the span input power per channel ( $P_{\text{IN SPAN}}$ ) for both the SC and WDM configurations and the two modulation formats under study. We notice first that the SC configuration is better than the WDM one from approximately one BER decade, while  $\sim 1$  dB more power per channel can be injected into the spans. It clearly means that the cross-phase modulation (XPM) and its related cross-polarization modulation (XPoIM) exacerbated by the WDM scheme badly impact the WDM transmission. In the SC configuration, only the self-phase modulation (SPM) excited at the locations of the high peak power impacts the

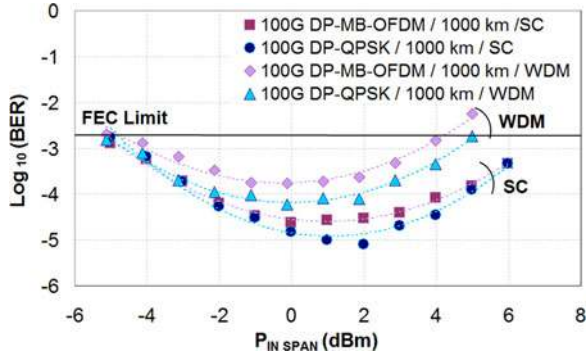


Fig. 8 BER versus channel span input power ( $P_{IN\ SPAN}$ ) of the 100 Gbps DP-MB-OFDM and 100 Gbps DP-QPSK modulation formats, in the single-channel (SC) and WDM configurations.

transmission performance. In the WDM configuration, the interplay between the high peak power in the neighboring channels (through XPM and XPolM) adds an extra penalty to the WDM system performance. When we now compare the two modulation formats between them, we notice that in the SC configuration, after the 1000-km transmission, the 100 Gbps DP-QPSK channel ( $BER \sim 1 \times 10^{-5}$  at  $P_{IN\ SPAN} \sim 1$  dBm) is a little better than the 100 Gbps DP-MB-OFDM channel ( $BER \sim 2.4 \times 10^{-5}$  at  $P_{IN\ SPAN} \sim 0$  dBm) both in terms of BER and optimal span input power. Also, in the WDM configuration, DP-QPSK ( $BER \sim 6 \times 10^{-5}$  at  $P_{IN\ SPAN} \sim 0$  dBm) is still slightly better than DP-MB-OFDM ( $BER \sim 2 \times 10^{-4}$  at  $P_{IN\ SPAN} \sim 0$  dBm). This indicates a slightly higher sensitivity of 100 Gbps DP-MB-OFDM to nonlinear effects when compared to 100 Gbps DP-QPSK. The exacerbation of four-wave mixing (FWM) that occurs between OFDM sub-carriers [27], [28] and between the OFDM sub-bands is probably the source of this slightly higher sensitivity to nonlinearities. However, in the present case of uncompensated transmission line, this effect is controlled by the continuous accumulation of chromatic dispersion along the line: the phase matching conditions which are mandatory to exacerbate intra and inter-band FWM are rarely met, which limits the FWM impact [29].

#### IV. ULTRA-NARROW PASS-BAND AND STOP-BAND OPTICAL FILTERS

A double target is followed for the design and building of optical pass-band and stop-band filters used in the sub-wavelength optical switch. They have to be ultra-selective to extract and suppress OFDM sub-bands as narrow as 8 GHz, while having a transfer function as rectangular as possible in order not to distort too much the neighboring sub-bands. Free-space optical (FSO) technology, based on bulk diffraction grating and filtering slit, is particularly adapted to ultra-narrow optical filtering [30], and permits to obtain typical full-width-half-maximum (FWHM) of 10 GHz and edge roll-off of 1000 dB/nm. The tunability of the filter central wavelength and bandwidth, authorized by the FSO approach, constitutes also an important feature of the developed devices. Note that optical filters based on fibre Bragg gratings can be as selective and steep as FSO-based filters, but with

TABLE I  
TYPICAL FEATURES OF THE PASS-BAND AND STOP-BAND OPTICAL FILTERS

	Optical Pass-Band Filter	Optical Stop-Band Filter
Insertion Loss	5 dB typical	5.5 dB typical
Edge roll-off	> 800 dB/nm	> 750 dB/nm
3-dB Bandwidth	32 pm / 4 GHz	65 pm/8 GHz
Isolation	60 dB typical	Not Applicable
Rejection	Not Applicable	60 dB typical

limited tunability capabilities [31]. From their side, wavelength selective switch, based on combination of diffraction grating and liquid crystal on silicon matrix, cannot reach the same spectral selectivity than FSO-based filters [32].

The optical pass-band and stop-band filters employ the same basic architecture. The main difference comes from the filtering slit, which is specific either to the pass-band or to the stop-band filter. The filter architecture is shown in Fig. 9 below, and is now detailed. The input divergent beam coming from the In/Out single mode fiber is collimated thanks to a lens, whose focal point is adjusted on the In/Out fiber. The filter architecture uses a polarization-diversity configuration in order to deal with the X and Y polarizations independently. A PBS separates the two polarization components and generates two elementary parallel light beams. A half wave-plate inserted over the lower beam turns its polarization by  $90^\circ$ . The diffraction grating is thus fed by two beams polarized in a direction perpendicular to the grating grooves. An optical expander is inserted before the grating, in order to spread the beams on the whole grating length and to maximize the separation strength of the Littman-Metcalf setup. A dihedron is placed after the grating as a retro-reflector, to increase the resolution of the device by doubling the number of passage into the grating. The beams are then sent to the upper filtering stage, and are finally focused onto a concave mirror, after passing through a slit. The role of this slit is to filter the signal either in the pass-band or stop-band configuration. The slit is fixed over a translation stage and can be moved into the beam: it allows changing the bandwidth of the filters. The filter central frequency is chosen thanks to a rotation of the retro-reflector. In the case of the pass-band filter, the slit shape is triangular. Note that the concave mirror has limited dimensions in the dispersion plane. Thus, the wavelengths corresponding to the beam portion reflected onto the concave mirror and not stopped by the slit are re-coupled on the way back in the In/Out fiber. This last one is connected to a circulator, which enables to decorrelate the input from the output signals. The optical configuration chosen here is symmetrical when considering the input and output beams, that in turn results in very low polarization dependant losses (PDL) for both the optical pass-band and stop-band filters. The typical PDL is equal to 0.2 dB and is mainly due to the circulator. Table I gives the main optical features of the developed filters. Their insertion losses do not exceed 5 dB for the pass-band filter and 5.5 dB for the stop-band filter. Their edge roll-off are typically higher than 800 dB/nm for the pass-band filter and 750 dB/nm for the stop-band filter. The minimum 3-dB bandwidth is equal to 32 pm (or 4 GHz) for the pass-band filter and 65 pm (or

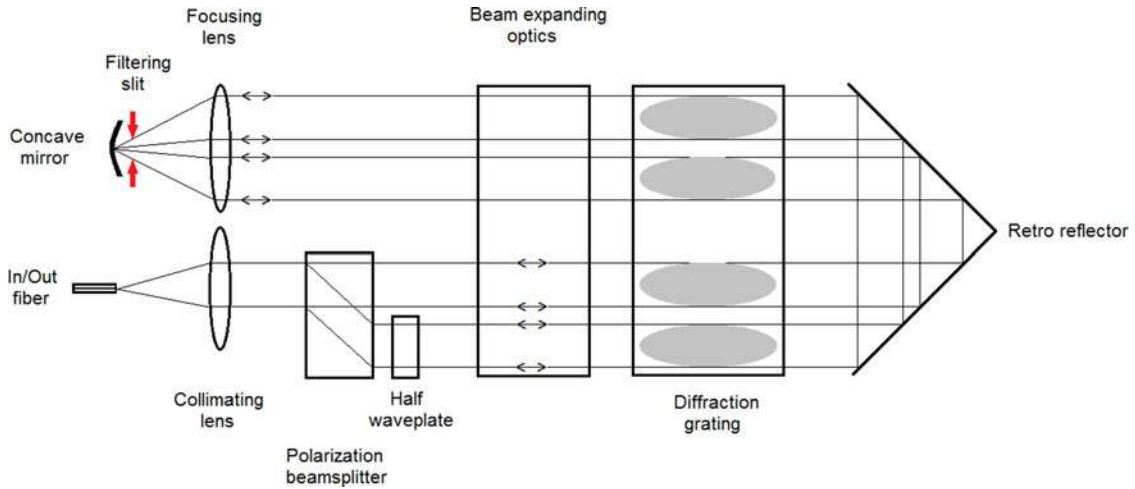


Fig. 9 Typical architecture of the ultra-narrow pass-band and stop-band optical filters used in the FOADM.

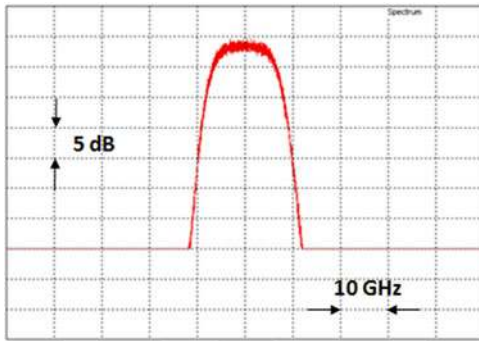


Fig. 10 Typical transfer function of the optical pass-band filter when its 3-dB bandwidth is  $\sim 14$  GHz.

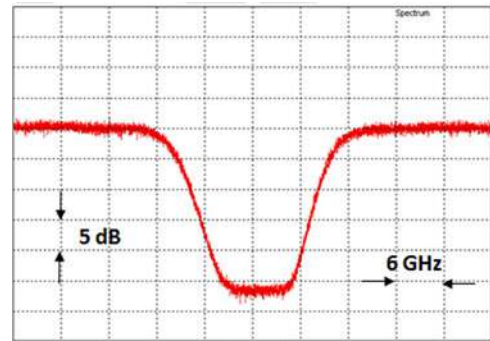


Fig. 12 Typical transfer function of the optical stop-band filter when its 3-dB bandwidth is  $\sim 20$  GHz.

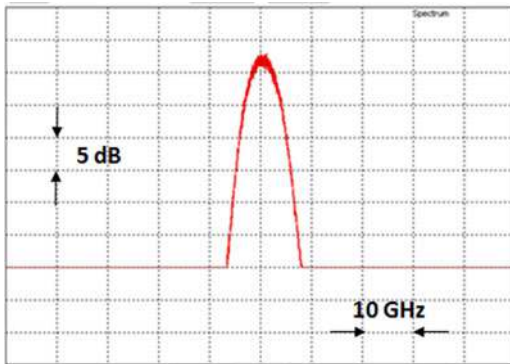


Fig. 11 Typical transfer function of the optical pass-band filter when its 3-dB bandwidth is  $\sim 4$  GHz.

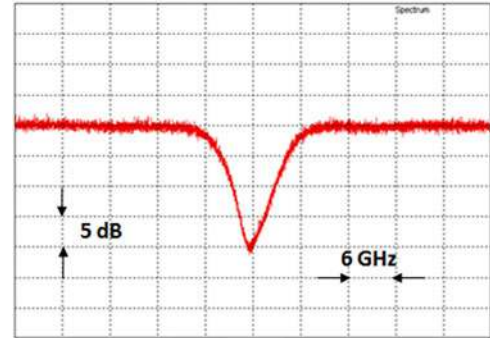


Fig. 13 Typical transfer function of the optical stop-band filter when its 3-dB bandwidth is  $\sim 10$  GHz.

8 GHz) for the stop-band filter. The isolation of the pass-band filter and rejection of the stop-band filter are typically 60 dB.

Figs. 10 and 11 present the typical profiles of the pass-band optical filter for 3-dB bandwidths equal to  $\sim 14$  and  $\sim 4$  GHz, respectively. For the 14-GHz bandwidth, the filter is nearly rectangular. Reduction of its bandwidth up to 4 GHz involves a modification of its profile, which becomes Gaussian. Figs. 12

and 13 shows the typical transfer function of the stop-band optical filter for 3-dB bandwidths of  $\sim 20$  GHz and  $\sim 10$  GHz, respectively. While the “notch” function is nearly rectangular when the 3-dB bandwidth is  $\sim 20$  GHz, it becomes triangular when the 3-dB bandwidth is decreased up to  $\sim 10$  GHz. Further reduction of the filter bandwidth is limited by several factors: firstly, the slit size cannot be reduced indefinitely and have to be

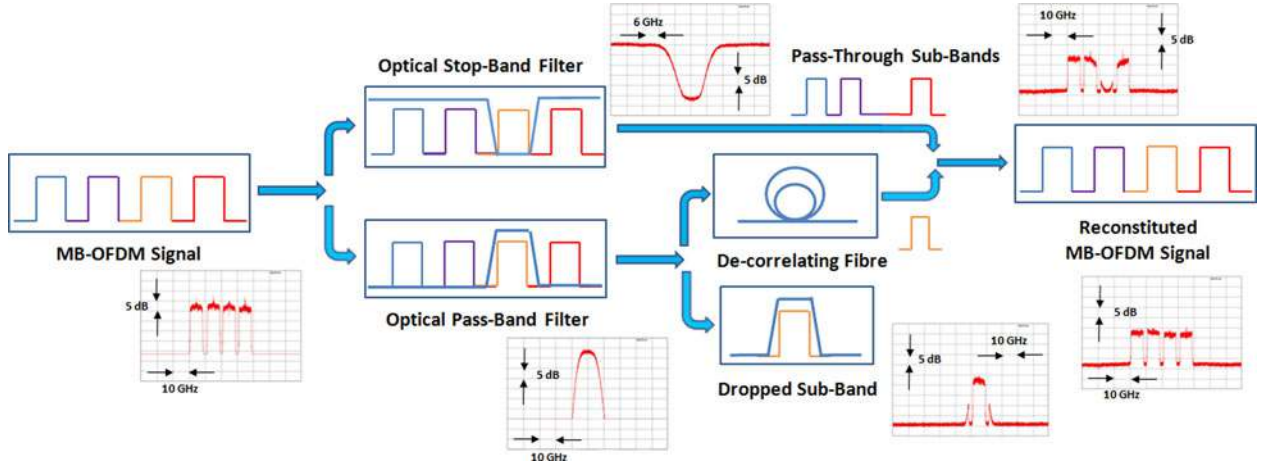


Fig. 14 Set-up of the OFDM sub-band optical add-drop multiplexer with the spectra of signals and optical filters in insets.

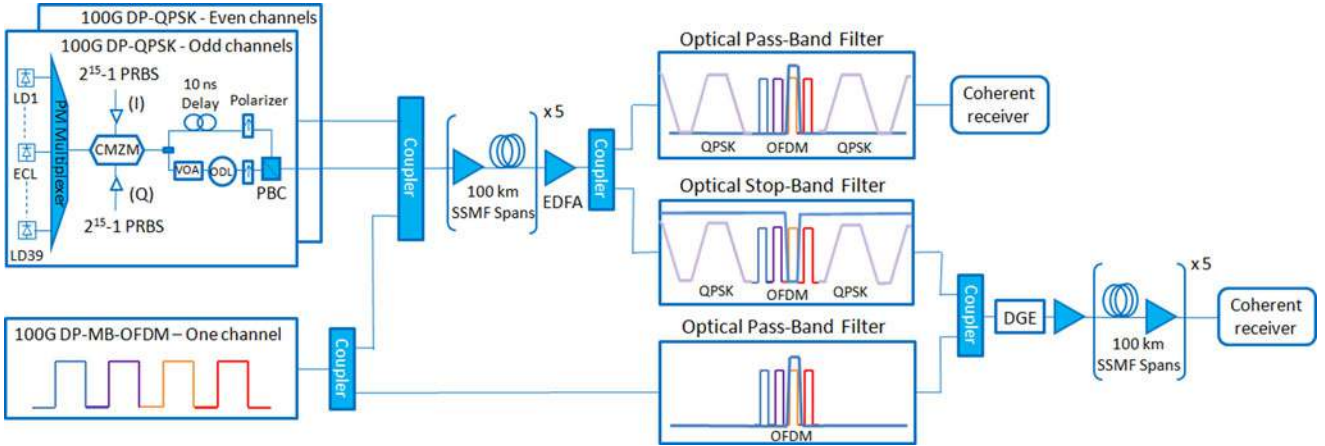


Fig. 15 Set-up of the  $10 \times 100$ -km transmission test-bed, with the 124.4 Gbps DP-MB-OFDM channel, the 79 odd and even 112 Gbps DP-QPSK wavelengths, the  $10 \times 100$ -km uncompensated G.652 SSMF transmission line with the sub-wavelength optical switch located in its middle.

higher than  $20 \mu\text{m}$ ; secondly, limitation over the number of lines of the diffraction gratings limits the grating dispersion strength; and finally, chromatic and spherical aberrations affecting optics degrade the resolution of the filters.

## V. OFDM SUB-BAND OPTICAL SWITCHING

We are now introducing our sub-band optical switch into the experiment [4]. Fig. 14 depicts the structure of our FOADM. The OADM is constituted of a first 3-dB coupler associated with an optical pass-band filter (OPBF) over its lower arm and an optical stop-band filter (OSBF) over its upper arm. In our experiment, the OSBF removes the third OFDM sub-band of the 100 Gbps DP-MB-OFDM signal, while the OPBF selects it. Once dropped, the third OFDM sub-band enters into another 3-dB coupler, whose lower arm is connected for instance to a coherent receiver and upper arm feeds a 5-km fiber spool. The role of this fiber spool is to de-correlate the signals once the third sub-band will be reinserted into the remaining truncated OFDM multiplex. The “add” operation is carried out by connecting the

de-correlating fiber to the OSBF output, as shown in Fig. 14. The spectrum of the OFDM signals and filter shapes are measured with a high-resolution (20 MHz) optical spectral analyzer [33] and shown in the insets of Fig. 14. In the back-to-back configuration, the OADM is inserted between the DP-MB-OFDM transmitter and the coherent receiver. In the transmission configuration, as shown in Fig. 15, the OADM is introduced in the middle of the previously depicted transmission line after the fifth SSMF spans. A 3-dB coupler located at the transmitter side firstly duplicates the 100 Gbps DP-MB-OFDM signal into two identical copies. The first signal replica is combined with the 79 odd and even 100 Gbps DP-QPSK channels and launched into the first five SSMF spans. After an EDFA, a 3-dB coupler sends the WDM multiplex firstly towards an OPBF in order to proceed to the “drop” of the third OFDM sub-band, and secondly towards the OSBF which removes the third OFDM sub-band from the OFDM multiplex. The second replica of the DP-MB-OFDM signal (generated at the transmitter side) is filtered by a second OPBF, which selects the third OFDM sub-band. Thanks to a third 3-dB coupler, this sub-band is re-injected into the trun-

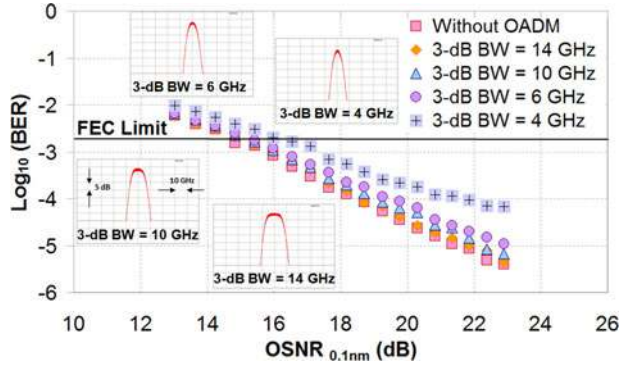


Fig. 16 BER versus OSNR of the sub-band 3 for various 3-dB BW of the OPBF, with the shapes of the OPBF for various 3-dB BW in insets.

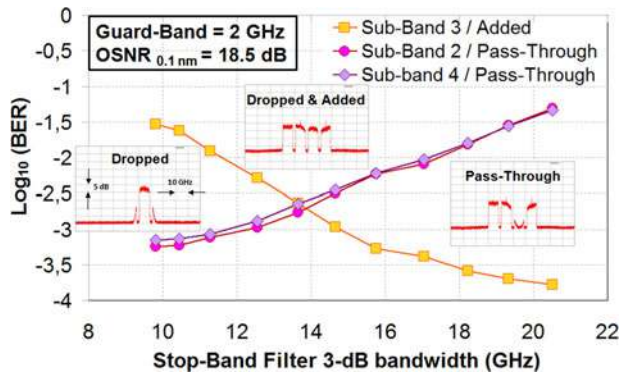


Fig. 17 BER versus 3-dB BW of the OSBF for the sub-bands 2, 3 and 4 and a GB = 2 GHz. In insets, the spectra of the signals at the optimum.

cated OFDM multiplex at the place of the sub-band, which has been removed by the OSBF. Note that here it is not necessary to use a de-correlating fiber before the “add” operation, as 500 km of fiber separate the added sub-band from the truncated OFDM multiplex (which receives this sub-band). After a DGE, the mix of 100 Gbps DP-MB-OFDM and 100 Gbps DP-QPSK channels is sent into the last five SSMF spans of the transmission link.

Our FOADM is firstly evaluated in back-to-back. The BER versus OSNR sensitivity curves are measured by degrading the OSNR thanks to a white noise source, which is coupled with the DP-MB-OFDM signal. Fig. 16 below gives the BER of the dropped sub-band (the third one) versus the OSNR in 0.1 nm for various 3-dB bandwidths (3-dB BW) of the OPBF. From 14 GHz to 6 GHz, the OSNR penalty is acceptable compared to the case where no OADM is inserted, but an error floor at  $BER \sim 1 \times 10^{-4}$  appears for a 3-dB BW of 4 GHz. In the following, we choose the 3-dB BW of 10 GHz for the “drop” OPBF, which results in a very low OSNR penalty with respect to the reference case without OADM.

Then, we plot in Fig. 17 the BER of the sub-bands 2, 3 and 4 as a function of the 3-dB BW of the OSBF after the “add-drop” operation when the guard-band (GB) is 2 GHz and OSNR = 18.5 dB (OSNR required for having a  $BER = 10^{-4}$  without OADM for the 100 Gbps DP-MB-OFDM signal). The impact of the

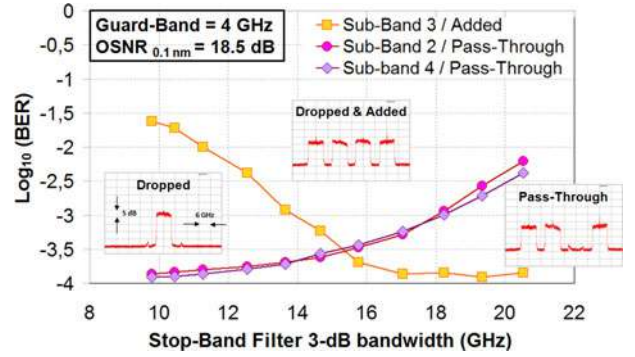


Fig. 18 BER versus 3-dB BW of the OSBF for the sub-bands 2, 3 & 4 and a GB = 4 GHz. In insets, the spectra of the signals at the optimum.

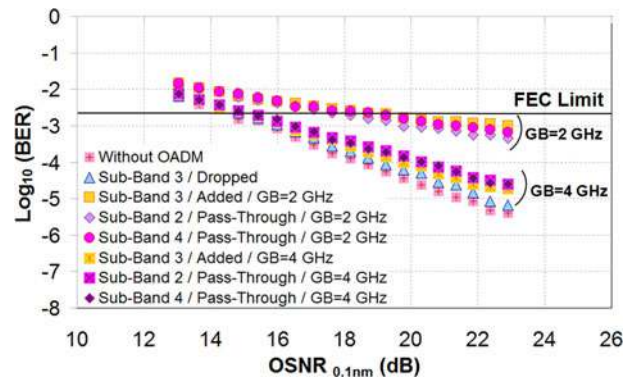


Fig. 19 BER versus OSNR of sub-bands 2, 3 and 4 in BtB (OADM inserted between the Tx and Rx) for a GB = 2 GHz and GB = 4 GHz.

crosstalk over the sub-band 3, between the added and remaining residual signals, is maximum (respectively, minimum) at low (respectively, at high) 3-dB BW of the OSBF. It is the opposite observation for the “pass-through” sub-bands 2 and 4, for which a large OSBF results in high spectral distortions. The optimum OSBF 3-dB BW results from a trade-off between the distortions affecting sub-band 3 from one side and sub-bands 2 and 4 from the other side, and is obtained at the intersection of these three measured curves. For a GB = 2 GHz, the optimum OSBF 3-dB BW is equal to  $\sim 14$  GHz, while the BER of sub-bands 2, 3 and 4 is  $\sim 3 \times 10^{-3}$ .

The same measurements have been carried out in Fig. 18 for a GB = 4 GHz and OSNR = 18.5 dB. The optimum 3-dB BW is now equal to  $\sim 15.7$  GHz, while the BER of sub-bands 2, 3 and 4 has been improved up to  $\sim 3 \times 10^{-4}$ , i.e., one BER decade better than the BER previously obtained for the GB = 2 GHz.

In Fig. 19 is now plotted the BER of the dropped sub-band 3, added sub-band 3 and “pass-through” sub-bands 2 and 4 as a function of the OSNR for the optimum tunings of the OPBF and OSBF, obtained with the GB of 2 and 4 GHz. While the BER of the various sub-bands reaches a  $\sim 10^{-3}$  error floor (near from the FEC limit fixed here at  $BER = 2 \times 10^{-3}$ ) at high OSNR for a GB = 2GHz, the BER results are satisfying for a GB = 4 GHz. The corresponding OSNR penalty compared to the case “without OADM” is less than 1 dB at  $BER = 10^{-3}$ .

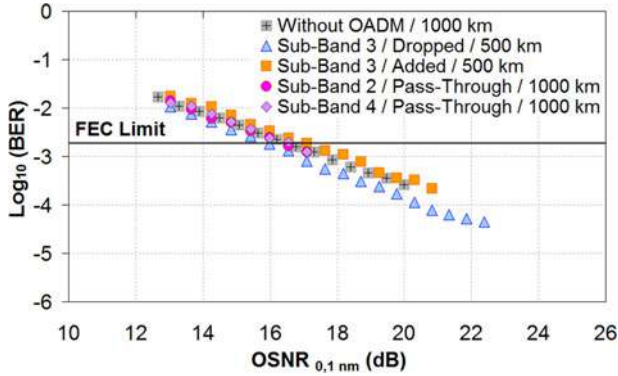


Fig. 20 BER versus OSNR of sub-bands 2, 3 & 4 after transmission (OADM inserted after 500 km) for a GB = 4 GHz.

It is the reason why we now evaluate the performance of our FOADM in the transmission line previously depicted with a GB tuned over the 4-GHz value. Results are presented in Fig. 20 by the means of BER versus OSNR sensitivity curves for the sub-bands 2, 3 and 4. Previously implemented experiments over the  $10 \times 100$ -km transmission line without the OADM (see Fig. 8) show that the optimum channel span input power is  $\sim 0$  dBm, while the corresponding BER and OSNR are  $\sim 2 \times 10^{-4}$  and  $\sim 20$  dB, respectively. Note that this optimum power per channel is kept hereafter. Firstly, as a reference, the OSNR sensitivity curve of the 100 Gbps DP-MB-OFDM signal transmitted over the  $10 \times 100$ -km transmission line without the OADM is plotted. The performance of the sub-band 3, dropped after 500 km, and reinserted in the last 500-km of the link (after having been duplicated at the transmitter side) is measured, as well as the performance of the “pass-through” sub-bands 2 & 4 (which are transmitted over 1000 km on the ten SSMF spans). One can notice first that a negligible OSNR penalty is observed at  $\text{BER} = 10^{-3}$  whatever the configuration tested, and secondly that the BER obtained at the best OSNR (measured when the white noise source is not activated) is below the FEC limit for the dropped, added and “pass-through” sub-bands. Note that the best achievable OSNR on the sensitivity curves differ as a function of the configuration considered, since the transmission distance and accumulated ASE are different.

## VI. CASCADABILITY OF THE SUB-BAND OPTICAL SWITCH

The question of the cascability of the previously defined FOADM is now studied thanks to the insertion of the add-drop multiplexer into a  $2 \times 100$ -km G.652 fiber-based recirculating loop. The guard-band between the OFDM sub-bands is still fixed at 4 GHz. The 3-dB bandwidths of the OPBF and OSBF are equal to 10 GHz and 15.7 GHz, respectively, as previously optimized. The impact over the sub-band 3 (the sub-band which is dropped and reinserted) but also over the neighboring sub-bands 2 and 4 of the cumulated filtering transfer function as well as the crosstalk inside the OADM is investigated. Into the recirculating loop, the architecture of the OADM is identical to the one depicted in Fig. 14. After a 3-dB coupler, the

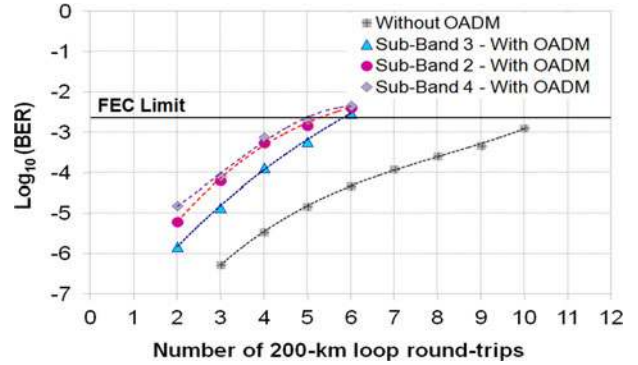


Fig. 21 BER versus number of  $2 \times 100$ -km loop round-trips for the sub-bands 2, 3 and 4, when the OADM is inserted or not into the loop.

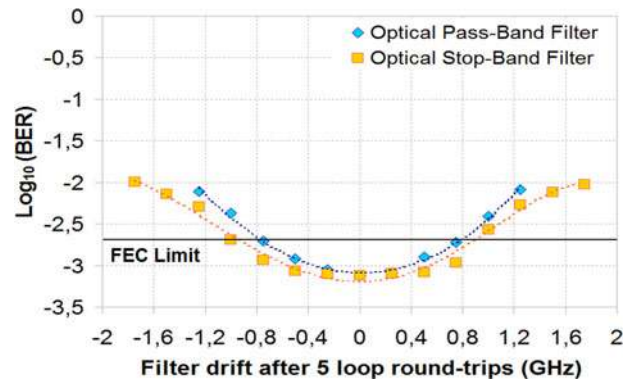


Fig. 22 BER versus OPBF and OSBF central frequency drifts for the sub-band 3 after 5 loop round-trips (or 1000 km).

100 Gbps DP-MB-OFDM signal is filtered by a OPBF (respectively, OSBF) which extracts (respectively, removes) the sub-band 3 from the OFDM multiplex. After a 5-km de-correlating fiber, the OPBF and OSBF outputs are re-coupled together, and the reconstituted OFDM multiplex with the “pass-through” and “added” sub-bands is sent into the loop for a new round-trip. This OADM configuration allows us evaluating the impact of the repeated action of the OPBF and OSBF over the OFDM signal (more particularly over the sub-band 2, 3 and 4), both in terms of filtering and crosstalk.

Fig. 23 below describes the experimental set-up. The transmitter, depicted in Fig. 6 and in Fig. 15, which mixes the 124 Gbps DP-MB-OFDM and the 79 odd and even 112 Gbps DP-QPSK, is connected to the recirculating loop through an acousto-optical modulator (AOM). The loop is constituted of two 100-km spans of G.652 fiber. An EDFA with 20-dB gain and 4.2-dB NF is located at the span input and output, as shown in Fig. 23 below. The OADM described above is then inserted into the loop. The sub-band 3 is firstly dropped and finally reinserted into the OFDM multiplex. It experiences thus the effect of the repeated action of the OPBF (over the “drop” path) and OSBF (over the “stop” path) transfer function, as well as the crosstalk coming from the interaction between the “drop” and “stop” paths. From their side, the sub-bands 2 and 4 experience

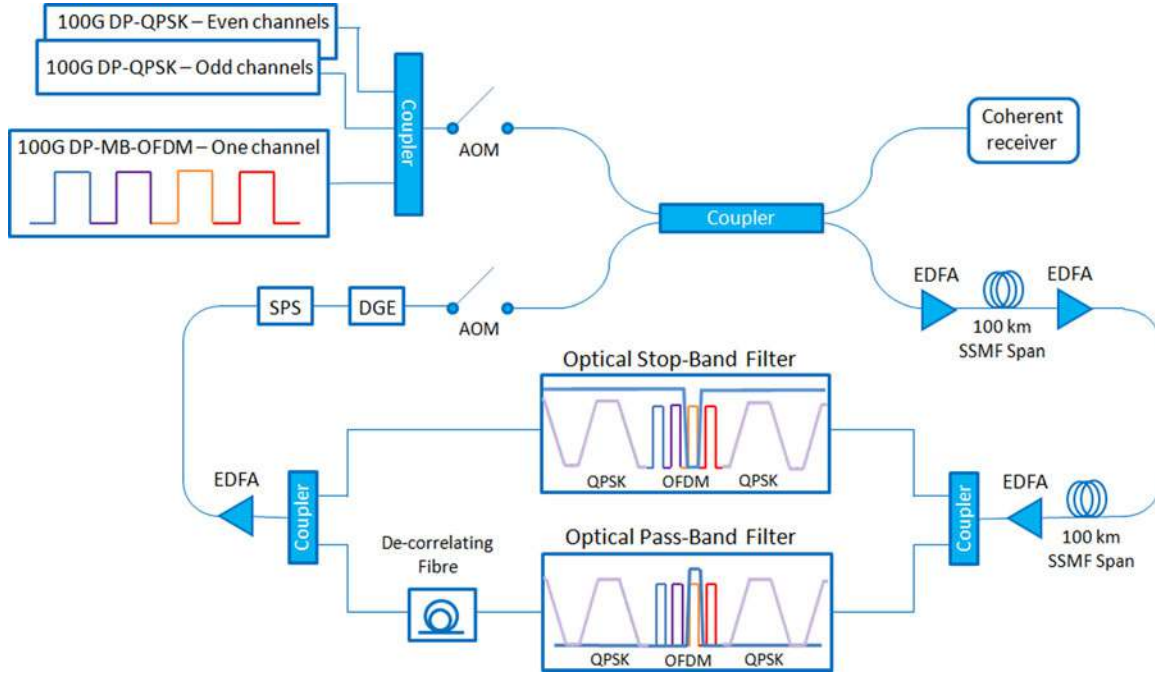


Fig. 23 Set-up of the  $2 \times 100$ -km G.652 fiber-based recirculating loop including the OFDM sub-band optical switch. AOM = Acoustic-Optical Modulator, SPS = Synchronous Polarization Scrambler, DGE = Dynamic Gain Equalizer.

the repeated distortions of the OSBF. An EDFA compensates for the introduced OADM losses. A DGE and a synchronous polarization scrambler (SPS) achieve power equalization and polarization rotation of the WDM multiplex after each loop round-trip, respectively. The role of the SPS is to stabilize the loop operation. Note that EDFA used in this Section VI are better than those used in the previous experiments ( $NF = 4.2$  dB here against  $NF = 5.5$  dB before), as the objective here is to cascade the highest possible number of OADM.

The performance of sub-bands 2, 3 and 4 is shown in Fig. 21. The BER is plotted as a function of the number of loop round-trips. For each transmission distance, the span input power per channel is optimized. Two configurations are studied. The case for which no OADM is inserted into the loop is taken as reference. The FEC limit (fixed here at  $BER = 2 \times 10^{-3}$ ) is reached after 10 loop round-trips or 2000 km. When the OADM is introduced into the loop, the BER of sub-band 3 ( $BER \sim 6 \times 10^{-4}$ ) after five round-trips or 1000 km, including the crossing of five OADM, is well below the FEC limit. The BER of sub-bands 2 and 4 ( $BER \sim 1.5 \times 10^{-3}$ ) is slightly worse than that of sub-band 3. Nonetheless, five loop round-trips can be achieved as well. This BER degradation with respect to sub-band 3 comes from the higher distortions which affect the edge sub-carriers of sub-bands 2 and 4 when compared to those of sub-band 3. Indeed, as indicated in the Table I, the edge roll-off of the OSBF ( $\sim 750$  dB/nm) and its corresponding frequency selectivity are lower than those of the OPBF ( $\sim 800$  dB/nm). The bandwidths of the OPBF and OSBF would have deserved to be re-optimized after each new loop round-trip. However, the performance improvement (respectively, degradation) for the sub-bands 2 and

4 (respectively, for the sub-band 3) would have been limited to less than  $\frac{1}{2}$  BER decade (as Fig. 21 lets it imagine), and no more than five loop round-trips would have been possible. To exhibit the progressive distortion affecting the sub-bands 2, 3 and 4, the spectrum of the MB-OFDM channel after each loop round-trip is also shown in Fig. 24.

The sensitivity to frequency drift of such ultra-narrow optical pass-band and stop-band filters is also a crucial question when considering their deployment in the field. Indeed, the mechanical or temperature stability of these devices is not as well ensured in the field as in the laboratory. Fig. 22 presents the BER evolution of the sub-band 3 (on which the “add-drop” operation is achieved) as a function of the OPBF and OSBF central frequency drift after five loop round-trips. In the OPBF case, the FEC limit is reached for absolute values of frequency drift higher than 0.8 GHz, which represents 20% of the OFDM signal bandwidth (fixed here at  $\sim 8$  GHz) if we consider the whole acceptance window going from  $-0.8$  to  $+0.8$  GHz. When considering now the OSBF, the acceptance window spreads from  $-1$  GHz up to 0.8 GHz, namely 22.5% of the OFDM signal bandwidth. Consequently, the sensitivity of the OFDM signal (here the sub-band 3) to the central frequency drift of the optical filters is slightly higher in the case of the OPBF than in the case of the OSBF. As expected, these values are relatively small, and will require that the optical filters be immunized against both mechanical vibrations and temperature variations.

These results are very encouraging when considering the introduction of such flexible OADM into meshed optical transport networks, for which several OADM (4 or 5) are often cascaded over a given path.

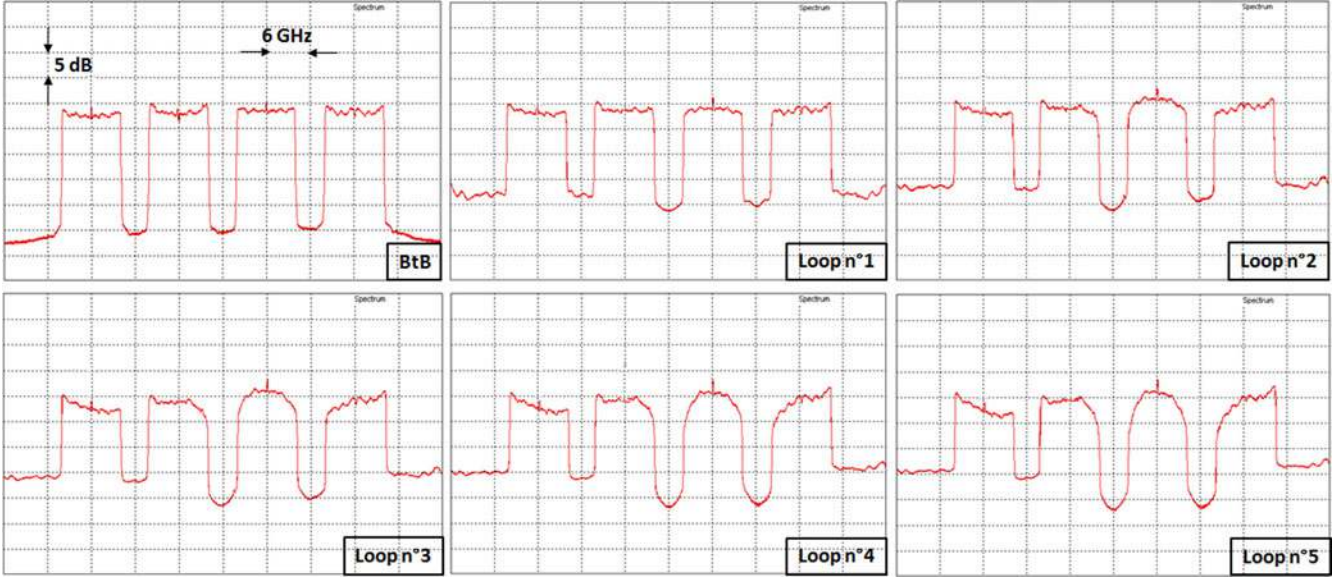


Fig. 24: Evolution of the 124.4 Gbps MB-OFDM channel spectrum measured with the high-resolution (20 MHz) OSA after each loop round-trip.

## VII. TYPICAL USE CASE FOR THE INTRODUCTION OF OFDM SUB-BAND OPTICAL SWITCHING IN THE NETWORK

The efficiency of ultra-narrow sub-wavelength optical switching has been extensively demonstrated above. We now consider the applicability of this technology in a multi-layer transport network. More precisely, we aim to evaluate the benefit of the combined introduction of flexibility and multi-band transmission techniques over the capital expenditure (CAPEX) cost of a representative national multi-layer transport network [34]. We propose to compare different scenarios in order to highlight the advantages that flexibility and MB-OFDM provide in terms of capacity transported by the network, in terms of filling of communication connections through the various network layers (from optical to IP layer), and, as a consequence, in terms of CAPEX cost for the overall network. Scenario S0 serves as a reference and corresponds to the currently deployed optical transport networks at 100 Gbps which use coherent single-carrier 100 Gbps DP-QPSK channels and fixed 50-GHz ITU-T grid. Scenarios S1 and S2 correspond to the up-coming use case of flexible transport networks for which the optical channel capacity will be better adapted to the traffic demands in order to overcome as much as possible over-provisioning. From one hand, scenario S1 reflects the upper part of Fig. 1 which describes the Nyquist-WDM super-channel solution employing a mixed 37.5/50 GHz spectral grid. On the other hand, scenario S2 corresponds to what is exhibited in the lower part of Fig. 1 with the achievement of a fully flexible management of the fiber bandwidth thanks to the MB-OFDM and sub-wavelength optical switching technologies.

In order to obtain a holistic view and evaluation of the introduction of optical flexibility in a multi-layer transport network, we first model the network by considering its essential elements. A multi-layer transport network can be divided in two main macroscopic layers composed of different kinds of equipments,

as depicted in Fig. 25. A packet layer aggregating IP traffic is located above a transmission layer which aggregates both time-division-multiplexing (TDM) traffic and IP flows while multiplexing and transporting optical channel inside the optical fiber. From an organic architecture point of view, the packet layer uses IP routers, whereas the transmission layer uses ROADM (if we consider the S0 scenario) and FOADM (if we consider the S1/S2 scenarios). The right hand-side of Fig. 25 represents our functional generic multi-layer network architecture model, using client/server relationships between the various layers [35]. In the scenario S0, the transmission layer is constituted of two sub-layers: the “*Optical Channel*” sub-layer represents a WDM channel, while the “*Colored Fiber*” sub-layer stands for the multiplex of 80 WDM channels transmitted in the optical fiber. In the scenarios S1 and S2, the transmission layer is decomposed in three different sub-layers called “*Sub-Band*,” “*Super-Channel*” and “*Slotted Colored Fiber*,” respectively. The “*Sub-Band*” sub-layer performs the choice of the adequate modulation format and data-rate that can be carried by a sub-band (or equivalently by a sub-wavelength) as a function of the transmission reach of the service demand.

The sub-bands/sub-wavelengths coming from the “*Sub-Band*” sub-layer are then aggregated inside a super-channel in the “*Super-Channel*” sub-layer in order to create an adaptive transmission path whose capacity is well-adjusted to the traffic demand. The “*Super-Channel*” entity is autonomous and transports the traffic from a point A to a point B without undergoing any sub-band optical switching process. While the “*Colored Fiber*” sub-layer supports up to 80 WDM channels (or equivalently 80 spectral slots of 50 GHz) in the scenario S0, 320 spectral slots of 12.5 GHz and 400 spectral slots of 10 GHz (i.e., 4000 GHz or 32 nm of overall bandwidth) can be transported by the “*Colored Slotted Fiber*” sub-layer of the scenarios S1 and S2, respectively. In the scenario S1, the sub-bands which constitute the super-channel occupy three spectral

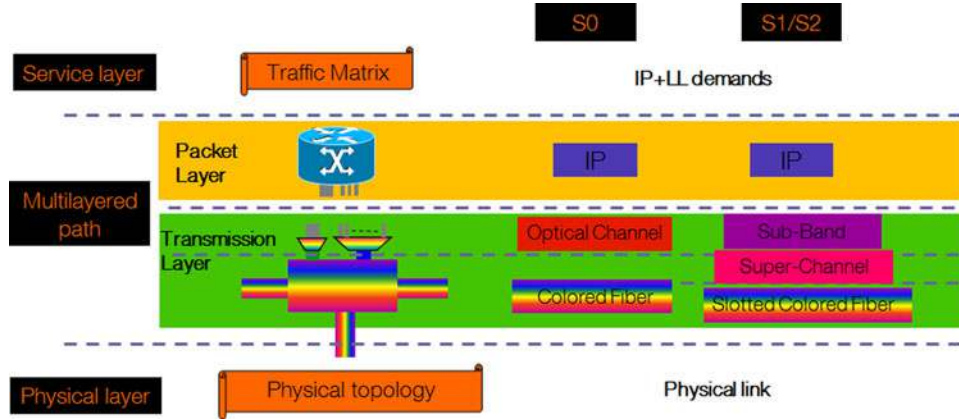


Fig. 25 Multi-layer transport network architecture with the details of the essential elements of the model. LL = Leased Line.

TABLE II  
DATA RATE AND MODULATION FORMAT ACHIEVED PER SPECTRAL SLOT FOR OUR THREE SCENARIOS WITH THE ASSOCIATED MAXIMUM TRANSMISSION REACH

Scenario	Data rate (Gbps)	Spectral slot (GHz)	Modulation format	Reach (km)
S0	100	50	DP-QPSK	2000
S1	50	37.5	DP-BPSK	4000
	100	37.5	DP-QPSK	2000
S2	200	37.5	DP-16QAM	400
	12.5	10	DP-BPSK	4000
	25	10	DP-QPSK	2000
	33.3	10	DP-8QAM	750
	50	10	DP-16QAM	400

slots of 12.5 GHz, namely 37.5 GHz overall. In the scenario S2, the OFDM sub-bands occupy a spectral slot of 10 GHz. All the transponders and muxponders used in the scenarios S1 and S2 are totally flexible and are able to generate any type of modulation format. Table II below summarizes the various options that can be considered in our three scenarios, in terms of data rate, modulation format and transmission reach supported by the “Optical Channel” or “Sub-Band” physical entity (or equivalently by the spectral slot of 50, 37.5 and 10 GHz for the scenarios S0, S1 and S2, respectively). Note that the transmission reach is determined by the choice of the modulation format and not by the choice of the scenario. In other words and as an example, a single-carrier WDM channel, a Nyquist-WDM or a MB-OFDM super-channel using for instance the QPSK modulation format will have the same maximum transmission reach (i.e., 2000 km). The maximum transmission distance considered in the Table II are obtained under the assumption that G.652 fiber is used over the transport network, soft-decision FEC (SD-FEC) is implemented into the transceivers and only EDFA are installed over the uncompensated transmission links of the network. They are fully compliant with what the equipment suppliers presently proposed [7], [8]. Furthermore, when no constraint exists over the transmission reach of a service demand, the modulation format having the best spectral efficiency (i.e., 16-QAM) is automatically preferred, involving in some

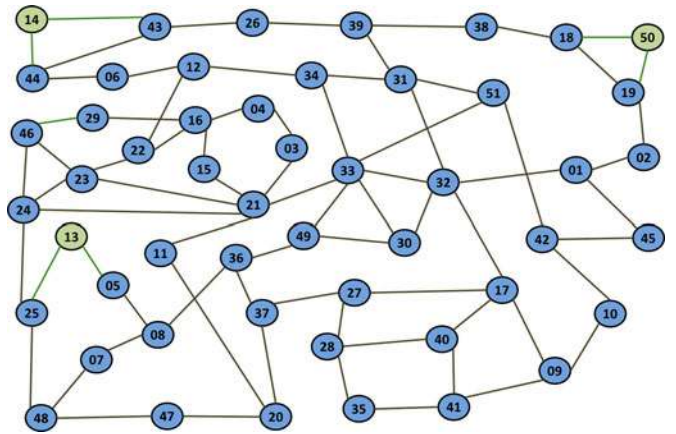


Fig. 26 Topology associated with the transport network studied here.

cases a substantial capacity over-provisioning but no CAPEX cost increase (by definition in our model).

Fig. 26 below shows the topology of the transport network used hereafter. It is representative of a transport backbone operated by a Tier-1 operator in a European country. The network is constituted of 51 nodes connected together thanks to 75 WDM links. The mean node degree is equal to 2.9. 80% of the links corresponds to transmission distances lower than 300 km. 25% corresponds to intra-city links and are shorter than 50 km. The average link length is equal to 217 km.

The traffic matrix associated with this network topology is composed of 371 demands divided into 185 IP demands and 186 leased-line (LL) demands (corresponding to TDM-based traffic) that represents globally more than 7 Tbps of ingress traffic. Although the number of IP and LL demands is quite equivalent, the part of the IP traffic volume into the global ingress traffic is twice more important than that of the LL demands. Note that the traffic demands in a real transport network are not uniformly spread over the nodes: some nodes are used for pure transit, while other nodes can manage up to 1 Tbps of edge services.

By sake of simplicity, we consider a global traffic matrix growth which does not make any difference between the TDM and IP-based services. In other words, the growing ratio is

identical for the IP and LL demands. In particular, complex traffic matrix evolutions integrating the apparition of new service demands along the time are not taken into account here. Instead of that, the variation of the traffic load is based on a yearly and fixed growing ratio of 35% whatever the type of demand. It constitutes a rather realistic assumption applicable to core transport networks where traffic is already largely aggregated. Three traffic volumes V1, V2 and V3 are considered, corresponding to a traffic projection for now, and for the next 4 and 7 years, respectively. As already mentioned, the scenario V1 corresponds to 7 Tbps of ingress traffic.

In this study, the routing of optical paths and the combined dimensioning of the various layers are optimized in order to make the global network cost as low as possible. An internally-developed multi-layer network optimization tool, based on a simulated annealing meta-heuristic, finds an adequate combination of the multi-layer paths yielding to a nearly optimal network cost. However, in this multi-layer network architecture environment, some dimensioning rules are required to map a client layer on a server layer. IP traffic is handled by IP routers, and the mapping of IP demands in the transmission layer is performed through the use of 10 and 100 GbE client interfaces. LL demands are managed directly by the transmission layer and are generated/detected by 10 and 100 GbE client interfaces, as well. The threshold to choose a 100 GbE interface rather than N-fold 10 GbE interfaces is fixed to 70 and 100 Gbps for IP and LL demands, respectively. For instance, if an IP path requires a bandwidth of 80 Gbps, a 100 GbE interface is installed in the IP router, rather than eight 10 GbE interfaces. At the opposite, if a LL path transports 80 Gbps, eight 10 GbE interfaces will be activated. Moreover, the dimensioning process does not integrate any resiliency mechanism, and corresponds to a “best fit” strategy that favors aggregation as much as possible. It means that “*Optical Channel*” sub-layer in scenario S0 can aggregate various IP/LL demands that are routed along the same physical path. In the scenarios S1 and S2, each IP/LL demand is allocated to a dedicated sub-band which is then incorporated into a super-channel. For instance, a traffic demand of 290 Gbps routed over a “*Slotted Colored Fiber*” of 300 km will use in the scenario S1 a super-channel composed of two sub-bands of 200 Gbps (with the DP-16QAM modulation format) occupying 7 slots of 12.5 GHz, i.e., six slots for the traffic itself and one additional slot for the guard-bands located from each side of the  $2 \times 200$  Gbps super-channel (as shown in the upper part of Fig. 1). In the scenario S2, the same demand will use a super-channel constituted of three sub-bands of 100 Gbps occupying six slots of 10 GHz. Note that in this last case, in accordance with what has been shown in the sections before, the guard-band is integrated into the 10 GHz spectral slot (with for instance, OFDM sub-bands of 8 GHz and guard-bands of 2 GHz from each side). Note as well that we consider here one super-channel entity per demand due to the fact that the super-channel is used as an aggregate of sub-bands, in order to adapt as finely as possible the allocated capacity to the traffic demand. Another way to proceed would be to consider super-channel as a dedicated switching layer in itself, able to groom any sub-band from any traffic demand. This will be studied into the on-going FP7 Eu-

TABLE III  
CONSIDERED COSTS FOR THE MAIN ELEMENTS OF THE MULTI-LAYER  
TRANSPORT NETWORK UNDER STUDY.

Item	Cost
<u>IP Router</u>	
Router (shelf and switch fabric)	1.62
10 GbE interface card	5.08
100 GbE interface card	8.42
<u>Directionless/Colorless OADM</u>	
OADM degree 1 (shelf and switch fabric)	2
OADM degree 2	12.36
OADM degree 3	17.87
OADM degree 4	23.77
Additional degree	34
10 GbE interface	0.04
100 GbE interface	4.17
100 Gbps WDM interface (Scenario S0)	8.33
12.5/10 GHz spectral slot (Scenarios S1/S2)	2.08

ropean project FOX-C [36]. However, if the “*Super-Channel*” sub-layer may make sense from an optical node implementation point of view, its benefits in terms of networking architecture is not obvious because it could introduce aggregation constraints.

For each iteration of the optimization process, the global network cost is inferred from the addition of the individual cost of the various network elements. The optimization is driven by the filling of the fiber in terms of spectral slot of 50, 37.5 and 10 GHz in the S0 and S1/S2 scenarios, respectively. When the maximum capacity of the fiber is reached, an additional degree is automatically added to the OADM node.

The Table III above presents the costs that are considered in our model for the most essential elements of our multi-layer transport network. The cost of the 12.5/10 GHz spectral slot in the scenarios S1/S2 is established as follows. We take as a reference the price of the flexible coherent WDM interface working at 100 Gbps and implementing both the Nyquist filtering and SD-FEC functionalities. We then make the two following assumptions: firstly we suppose that the cost ratio between this flexible coherent 100 Gbps WDM interface (operating indifferently over a 50 or 37.5 GHz spectral grid) and the 12.5/10 GHz spectral slot considered in the scenarios S1/S2 is equal to 4; secondly we assume that the price of a standard coherent 100 Gbps WDM interface considered in the scenario S0 with the SD-FEC functionality but without the Nyquist filtering is equal to the cost of this flexible coherent WDM interface working at 100 Gbps (at the expense of a slight over-estimation of its cost). Note at last that the cost difference between the flex-rate coherent WDM transceivers (for instance, between the 100 and 200 Gbps version of the flex-rate transceiver) comes uniquely from the embedded client interfaces whose number varies as a function of the data-rate addressed by the WDM part of the transceiver.

The results of our cost optimization for the multi-layer transport network previously described are presented in Fig. 27 for the three scenarios S0, S1, S2 and the three traffic matrix V1, V2, V3 under investigation. First of all, the cost of the packet layer is more or less the same whatever the considered scenario. It is the indication that IP traffic in transit is managed by the

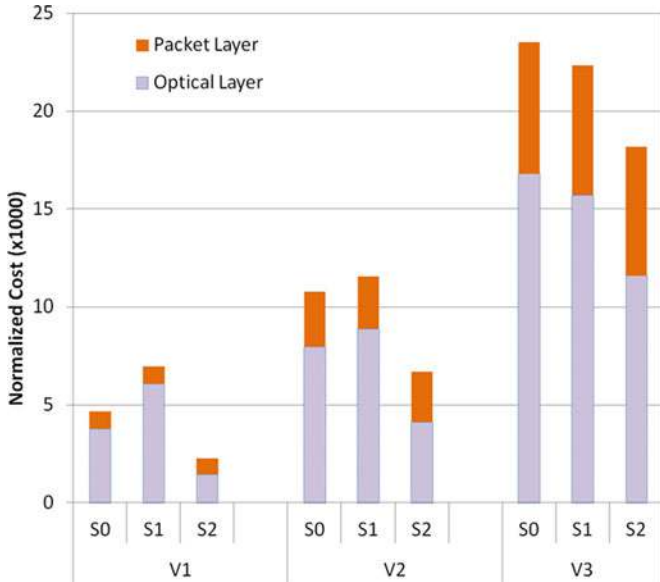


Fig. 27 Multi-layer transport network cost comparison in the scenarios S0, S1 and S2 for the traffic matrix V1, V2 and V3.

transmission layer and not by the packet layer, which is just used for the termination points of IP demands. Actually, the major part of the network cost is related to the transmission layer and optical transport, whatever the scenario (S1, S2, S3) and the traffic matrix (V1, V2, V3) considered. Any technique that permits to use more efficiently the fiber bandwidth is thus relevant for reducing the cost of the optical transport. With the traffic matrix V1, scenario S1 (which combines Nyquist-WDM technique and 37.5/50 GHz spectral grid) does not bring any benefit in terms of CAPEX cost reduction. Its cost is even  $\sim 50\%$  larger than that of the classical scenario (S0) using coherent 100 Gbps DP-QPSK channels and 50 GHz ITU-T grid. At the opposite, the scenario S2 combining MB-OFDM and sub-wavelength optical switching is dramatically better with a cost reduction of  $\sim 52\%$  when compared to scenario S0 and  $\sim 68\%$  when compared to scenario S1. These results prove very clearly all the potential of the MB-OFDM and sub-wavelength optical switching techniques to manage as efficiently as possible the fiber bandwidth. With the traffic matrix V2, scenario S0 is still  $\sim 7\%$  better than scenario S1, but  $\sim 28\%$  worse than scenario S2. With the highest traffic matrix V3, the flexible scenarios S1 and S2 are better than the scenario S0 with a CAPEX gain of  $\sim 5\%$  and  $\sim 23\%$ , respectively. The traffic matrix growth makes the use of Nyquist-WDM super-channels and 37.5/50 GHz spectral grid more relevant, because the traffic going from a point A to a point B becomes larger and the need for sub-wavelength optical switching is less stringent. The same explanation is valid for justifying that the cost reduction allowed by the scenario S2 becomes lower and lower when the traffic matrix increases. In consequence, the migration towards scenario S1 is not entirely justified in a short-term perspective, and implementation of the scenario S0 (coherent 100 Gbps DP-QPSK channels over a 50 GHz ITU grid) during the next 4 or 5 years is very pertinent. In all cases studied here, use of the scenario S2 (com-

bination of MB-OFDM and sub-wavelength optical switching techniques) is always relevant, and justify the effort made to design and build ultra-selective FOADM (as presented in this paper). Furthermore, in the context of a real transport network operation, the resources have to be regularly up-graded to support the traffic increase. The global network cost follows more or less the traffic growth evolution with the scenario S2, which is well-adapted to “a pay as you grow” investment model. This is due to the fact that the optical transport network dimensioning is finely adjusted to the traffic demands without any capacity over-provisioning. From their side, scenarios S0 and S1, which may allocate higher capacity than that required by the real traffic load, have the capacity to support smooth traffic increase without adding any new resources. It explains why the cost evolutions are more irregular with the scenarios S0 and S1 than with the scenario S2, when the traffic matrix increases. The cost evolution trends that we have highlighted there should be reinforced if we integrate the cost erosion parameters in our study. Note at last that end-to-end protection resiliency mechanisms have still to be integrated in our study to evaluate the total cost of the protected multi-layer transport network. Nonetheless, it could be reasonably assumed that the protected network cost will be slightly higher than two, as resources for service transport and protection are twofold more important, while protected routes (which can be longer than the original ones) could engender extra-cost related to the insertion of new regeneration sites.

## VIII. CONCLUSION

In this manuscript, we provide the experimental proof of concept of sub-band optical switching over a 100 Gbps MB-OFDM signal. After having demonstrated that 100 Gbps DP-MB-OFDM presented the same performance than 100 Gbps DP-QPSK on an uncompensated  $10 \times 100$ -km G.652 fiber-based transmission line, we successfully perform an optical “add-drop” of an OFDM sub-band as narrow as 8 GHz inside a 100 Gbps DP-MB-OFDM signal constituted of four sub-bands spaced by 4-GHz guard-bands. The essential elements of this FOADM are composed of two ultra-selective optical pass-band and stop-band filters whose rectangular shape and narrow bandwidth allowed OFDM sub-band extraction and suppression, respectively. The crucial question of the cascadability of such ultra-selective optical filters is addressed, by inserting our FOADM into a G.652 fiber-based recirculating loop. We prove that five OADM can be cascaded without degrading too much the transmission performance. Such demonstration opens the way to optical meshed transport networks with a high degree of flexibility. Indeed, the combination of MB-OFDM technique and sub-band optical switching allows to increase significantly the fiber throughput and to manage finely the fiber bandwidth, while adapting the optical connections (i.e. the OFDM sub-bands) to the transported services. As shown in the last part of this paper, another crucial advantage of this scheme is the ability to optimize the aggregation process in its multi-layer dimension (from the optical layer up to the IP layer), and in turn to make significant cost savings on the deployed equipments and, as a consequence, on the energy consumption (even if this point

has not been investigated here). Our proposal pushes network flexibility far away of what is today proposed by system vendors, opening new horizons for an optimized use of multi-layer transport networks.

## REFERENCES

- [1] A. Morea, O. Rival, N. Brochier, and E. Le Rouzic, "Data-rate adaptation for night-time energy savings in core networks," *J. Lightw. Technol.*, vol. 31, no. 5, pp. 779–785, Mar. 2013.
- [2] T. Zami, "What is the benefit of elastic superchannel for WDM network?," presented at the Eur. Conf. Exhib. Opt. Commun., London, U.K., 2013, Paper We.2.E.1.
- [3] R. Dischler, F. Buchali, and A. Klekamp, "Demonstration of bit rate variable ROADM functionality on an optical OFDM super-channel," presented at the Opt. Fiber Commun. Conf., San Diego, CA, 2010, Paper OTuM7.
- [4] E. Pincemin, M. Song, J. Karaki, A. Poudoulec, N. Nicolas, M. Van Der Keur, Y. Jaouen, P. Gravey, M. Morvan, and G. Froc, "Multi-band OFDM transmission with sub-band optical switching," presented at the Eur. Conf. Exhib. Opt. Commun., London, U.K., 2013, Paper Th.2.A.1.
- [5] A. Morea, J. Renaudier, A. Ghazisaeid, O. Bertran Pardo, and T. Zami, "Impact of reducing channel spacing from 50 GHz to 37.5 GHz in fully transparent meshed networks," presented at the Opt. Fiber Commun. Conf., San Francisco, CA, 2014, Paper Th1E.4.
- [6] T. Zami, "Interest of mix-grid setup for elastic spectral efficiency," presented at the 39th Eur. Conf. Opt. Commun., London, U.K., 2013, Paper P.5.5.
- [7] Corestream agility optical transport system brochure. [Online]. Available: [www.ciena.com](http://www.ciena.com).
- [8] 1830 photonic service switch brochure. [Online]. Available: [www.alcatel-lucent.com](http://www.alcatel-lucent.com).
- [9] C. Laperle and K. Roberts, "Flexible transceivers," presented at the Eur. Conf. Opt. Commun., Amsterdam, The Netherlands, 2012, Paper We.3.A.3.
- [10] S. Gringeri, E. B. Basch, and T. J. Xia, "Technical considerations for supporting data rates beyond 100Gbps," *IEEE Commun. Mag.*, vol. 50, no. 2, pp. 21–30, Feb. 2012.
- [11] S. L. Jansen, I. Morita, T. C. W. Schenk, N. Takeda, and H. Tanaka, "Coherent optical 25.8-Gb/s OFDM transmission over 4160-km SSMF," *J. Lightw. Technol.*, vol. 26, no. 1, pp. 6–15, Jan. 2008.
- [12] S. L. Jansen, I. Morita, T. C. W. Schenk, and H. Tanaka, "121.9-Gb/s PDM-OFDM transmission with 2-b/s/Hz spectral efficiency over 1000 km of SSMF," *J. Lightw. Technol.*, vol. 27, no. 3, pp. 177–188, Feb. 2009.
- [13] J. Armstrong, "OFDM for optical communications," *J. Lightw. Technol.*, vol. 27, no. 3, pp. 189–204, Feb. 2009.
- [14] Y. Tang and W. Shieh, "Coherent optical OFDM transmission up to 1 Tb/s per channel," *J. Lightw. Technol.*, vol. 27, no. 16, pp. 3511–3517, Aug. 2009.
- [15] Q. Yang, Y. Tang, Y. Ma, and W. Shieh, "Experimental demonstration and numerical simulation of 107-Gb/s high spectral efficiency coherent optical OFDM," *J. Lightw. Technol.*, vol. 27, no. 3, pp. 168–176, Feb. 2009.
- [16] T. M. Schmidl and D. C. Cox, "Robust frequency and timing synchronization for OFDM," *IEEE Trans. Commun.*, vol. 45, no. 12, pp. 1613–1621, Dec. 1997.
- [17] H. Minn and V. K. Bhargava, "A simple and efficient timing offset estimation for OFDM systems," in *Proc. Veh. Technol. Conf.*, 2000, pp. 51–55.
- [18] K. Shi and E. Serpedin, "Coarse frame and carrier synchronization of OFDM systems: A new metric and comparison," *IEEE Trans. Wireless Commun.*, vol. 3, no. 4, pp. 1271–1284, Jul. 2004.
- [19] J. Karaki, E. Pincemin, Y. Jaouen, and R. Le Bidan, "Frequency offset estimation robustness in a polarization-multiplexed coherent OFDM system stressed by chromatic dispersion and polarization mode dispersion," presented at the Conf. Lasers Electro-Opt., San Jose, CA, USA, 2012, Paper CF1F.3.
- [20] S. Jansen, I. Morita, T. C. W. Schenk, and H. Tanaka, "Long-haul transmission of  $16 \times 52.5$  Gbits/s polarization-division multiplexed OFDM enabled by MIMO processing," *J. Opt. Netw.*, vol. 7, pp. 173–182, 2008.
- [21] D. Petrovic, W. Rave, and G. Fettweis, "Effects of phase noise on OFDM systems with and without PLL: Characterization and compensation," *IEEE Trans. Commun.*, vol. 55, no. 8, pp. 1607–1616, Aug. 2007.
- [22] J. Karaki, E. Pincemin, Y. Jaouen, and R. Le Bidan, "First and second-order PMD impact over 100 Gbps polarization-multiplexed coherent MB-OFDM system under realistic "field" conditions," in *Proc. IEEE Photon.*, Arlington, VA, USA, 2011, pp. 831–832, Paper ThT4.
- [23] D. Godard, "Self-recovering equalization and carrier tracking in two-dimensional data communication systems," *IEEE Trans. Commun.*, vol. C-28, no. 11, pp. 1867–1875, Nov. 1980.
- [24] S. Savory, "Digital filters for coherent optical receiver," *Opt. Exp.*, vol. 16, pp. 804–817, 2008.
- [25] A. Leven, N. Kaneda, U. V. Koc, and Y. K. Chen, "Frequency estimation in intradyne reception," *Photon. Technol. Lett.*, vol. 19, pp. 366–368, 2007.
- [26] D. S. Ly-Gagnon, S. Tsukamoto, K. Katoh, and K. Kikuchi, "Coherent detection of optical quadrature phase-shift keying signals with carrier phase estimation," *J. Lightw. Technol.*, vol. 24, no. 1, pp. 12–21, Jan. 2006.
- [27] A.J. Lowery, S. Wang, and M. Premaratne, "Calculation of power limit due to nonlinearity in optical OFDM systems," *Opt. Exp.*, vol. 15, pp. 13282–13287, 2007.
- [28] M. Nazarathy, J. Khurgin, R. Weidenfeld, Y. Meiman, P. S. Pak, R. Noe, and I. Shpantzer, "The FWM impairment in coherent OFDM compounds on a phased-array basis over dispersive multi-span links," presented at the Coherent Opt. Technol. Appl., Boston, MA, USA, 2008, Paper CWA4.
- [29] M. Nazarathy, J. Khurgin, R. Weidenfeld, Y. Meiman, P. S. Pak, R. Noe, I. Shpantzer, and V. Karagodsky, "Phased-array cancellation of nonlinear FWM in coherent OFDM dispersive multi-span links," *Opt. Exp.*, vol. 16, pp. 4228–4236, 2008.
- [30] H. Lefèvre, "Rectangular response optical filter for partitioning a limited spectral interval," U.S. patent 6 832 022 B1, 2004.
- [31] WSS ROADMs product guide. [Online]. Available: [www.finisar.com](http://www.finisar.com).
- [32] Ultra-narrow-band tunable optical filter data sheet. [Online]. Available: [www.teraxion.com](http://www.teraxion.com)
- [33] High resolution optical spectrum analyzer AP2050 series data sheet. [Online]. Available: [www.apex-t.com](http://www.apex-t.com)
- [34] K. Christodoulouopoulos, I. Tomkos, and E. A. Varvarigos, "Elastic bandwidth allocation in flexible OFDM-based optical networks," *J. Lightw. Technol.*, vol. 29, no. 9, pp. 1354–1366, May 2011.
- [35] J. Berthold, A. A. M. Saleh, L. Blair, and J. M. Simmons, "Optical networking: Past, present, and future," *J. Lightw. Technol.*, vol. 26, no. 9, pp. 1104–1118, May 2008.
- [36] FP7 Call 8 FOX-C project, deliverable D21. [Online]. Available: <http://www.ict-fox-c.eu>